The extended peridynamic model for elasto-plastic and/or fracture problems

Wei-Jian Li[1,2,3] | Tao You[1,2,4] | Tao Ni[1,2] | Qi-Zhi Zhu*[1,2] | Leong Hien Poh[3]

[1]Key Laboratory of Ministry of Education for Geomechanics and Embankment Engineering, Hohai University, Nanjing 210098, China
[2]College of Civil and Transportation Engineering, Hohai University, Nanjing 210098, China
[3]Department of Civil and Environmental Engineering, National University of Singapore, 1 Engineering Drive 2, E1A-07-03, Singapore 117576
[4]Department of Environmental Informatics, Helmholtz Centre for Environmental Research-UFZ, Leipzig 04318, Germany

Correspondence
*Qi-Zhi Zhu, Email: qzhu@hhu.edu.cn

Summary

The strain-based implementation method for the extended peridynamic model (XPDM) resolves the limitation of standard models where only a fixed Poisson's ratio can be achieved. In this contribution, the XPDM formulation is extended to include bond breakage and/or plasticity mechanisms. The elasto-plastic and bond breakage algorithms are elaborated. To capture the fracture process, a shear mechanism is now incorporated to the bond breakage response, in addition to the standard stretching failure mode. It is shown that the shear mechanism is required to accurately reproduce mixed mode fracture behavior observed experimentally. To demonstrate the predictive behavior of the strain-based XPDM, a wide range of quasi-static and dynamic loading conditions, for both brittle and elasto-plastic materials, is considered against experimental results or practical engineering scenarios.

KEYWORDS:
Extended peridynamic model (XPDM), crack propagation, failure criteria, elasto-plastic fracture

1 | INTRODUCTION

Crack induced failure of geomaterials has long been the research focus in engineering science, where computational modeling has become an indispensable tool for understanding the mechanical behavior of solids before and after failure. As one of the most promising methods, peridynamic model has drawn much attention for its non-local formulation and meshless discretization framework [1,2,3]. The governing equations are reformulated through the integration of bond force density, such that difficulties with displacement discontinuity are circumvented [4,5,6,7,8,9,10]. It is thus commonly adopted for the modelling of fracture processes [11,12,13,14,15,16]. Recently, [17] proposed a peridynamic differential operator to construct nonlocal solutions of differential equations, extending the application of peridynamics to more areas [18,19,20,21]. The original bond-based peridynamic formulation by [4], however, can only describe a fixed Poisson's ratio. Moreover, the force density grows linearly with bond stretch until a threshold value, where the connection between two material points vanishes. Such a framework cannot adequately capture nonlinear failure responses, nor in situations with significant shear deformation. In this paper, we focus on the strain based extended peridynamic model (XPDM) developed in [22,23], which remedies the Poisson's ratio limitation, and extend it to incorporate shear breakage and elasto-plastic mechanisms, such that a wide range of complex fracture behavior can be accurately captured.

In the literature, several developments have been proposed to extend the range of applications with peridynamic models. To circumvent the fixed Poisson's ratio limitation, modified formulations include the ordinary state-based peridynamic model [24], the conjugated bond-based peridynamic model [25,26], as well as other related approaches [27,28,29,30,31,32,33,34,35]. Other researchers focus on the bond constitutive relations to capture the fracture response more adequately [36,37,38,39,40,41], though most work are restricted to brittle behavior. Such modifications may thus be inadequate in situations involving significant plastic deformation,

[0]**Abbreviations:** ANA

e.g. cohesive-frictional materials in compression dominated loading conditions. For the latter, an ordinary state-based peridynamic plasticity model was proposed in [42] where the yield function is constructed through the relationship between strain energy density and equivalent stress, as well as related model extensions by [43,44,45,46]. This allows the incorporation of the von mises yield criterion into the ordinary state based framework. In general, however, the incorporation of more complicated plasticity mechanisms into the peridynamic model, e.g. as functions of maximum shear stress / hydrostatic pressure / lode angle etc, can be challenging. One way to address this is to adopt the non-ordinary state-based peridynamic model [24], to incorporate local constitutive equations more easily. However, the numerical implementation may suffer from stability issues due to potential material penetration [47] and zero-energy mode oscillations [48,49]. Some researchers have proposed methods to deal with these deficiencies [50,51], though the resulting implementation becomes more complicated.

The extended peridynamic model by [22] remedied the Poisson's ratio limitation, by incorporating the bond rotational effect into the formulation. However, it was found that the proposed enrichment suffered from rigid body rotational effect, which was later addressed in [23] via a local strain-based implementation technique. Here, the enriched model is termed the XPDM, in which the bond rotational effect is captured via the bond shear strain. In XPDM, the macroscopic strain energy of peridynamic system is reformulated by introducing local shear deformation. It can be viewed as an extension to the classical bond-based central force peridynamic theory by incorporating bond shearing effect with an additional degree of freedom in the tangential direction. Thus the microscopic shearing mechanisms can be better considered in the XPDM framework.

While the XPDM has successfully resolved the Poisson's ratio limitation, prior work was limited to the linear regime or simple tensile fracture responses. This forms the motivation of the paper, which focuses on the extension of XPDM in static or dynamic loading conditions, for both brittle and elastoplastic fracture processes. Since the bond deformation can be derived from the local strain, a direct relationship between the nodal internal force and the local strain can be obtained through XPD bonds. Conceptually, this is similar to the relationship between the nodal forces and Gaussian strains in a finite element model: the product of the elastic bond deformation and the initial bond stiffness is analogous to the product of the elastic strain and the stiffness matrix of the latter. Therefore, in the XPDM framework, the nodal internal force can be directly obtained from the local elastic strain, which facilitates the direct use of classical elastoplastic models.

For modeling crack propagation, the critical stretch fracture criterion is the most commonly used criterion for brittle fracture in the bond-based model or even the state-based model [52,53], but the lack of shear mechanism consideration makes it inadequate for predicting crack propagations under compression. A peridynamic formulation of J-integral for the study of surface opening cracks was proposed in [54], though its predictive accuracy is influenced by the horizon size relative to the crack size. For the XPDM, a shear failure mechanism is introduced in the bond breakage relation in addition to the classical tensile failure criterion, to help capture the shear cracks observed in experiments. For elastoplastic fracture problems, a generalized stored energy function at the XPD bond level is proposed, with an emphasis on the determination of critical energy that induces fracture.

The paper is organized as follows: Section 2 describes the main constitutive equations of the XPDM. Section 3 incorporates the elastoplastic theory into the force density - strain constitutive relations. Section 4 presents two new bond failure criteria in XPDM. Section 5 provides the computational algorithm for both brittle and elastoplastic fracture analyses. In Sections 6, we illustrate the accuracy and effectiveness of the proposed method by benchmarking against nonlinear finite element results and experimental data.

2 | SUMMARY OF THE EXTENDED PERIDYNAMIC FORMULATIONS

For completeness, a summary on XPDM is provided. Detailed discussions can be found in [22,23]. In peridynamic theory, the local equilibrium condition is described via an integral term to describe the force density $\boldsymbol{f}(\boldsymbol{x})$ acting at that point. Following Newton's second law, the equation of motion at material point $\boldsymbol{x}$, instant t, can be written as [4]:

$$\rho\ddot{\boldsymbol{u}}(\boldsymbol{x},t) = \int_{\mathcal{H}_x} \boldsymbol{f}(\boldsymbol{x},t)\,\mathrm{d}V_{x'} + \boldsymbol{b}(\boldsymbol{x},t), \quad \boldsymbol{x}\in\Omega \tag{1}$$

where the integral term defines the resultant force density at point $\boldsymbol{x}$; ρ denotes density, $\ddot{\boldsymbol{u}}$ is the acceleration vector, and $\boldsymbol{b}$ is the body force density. The *horizon* associated with material point $\boldsymbol{x}$ is denoted as $\mathcal{H}_x$ with the parameter δ describing the material horizon, as shown in Figure 1.

2.1 | Local constitutive equations

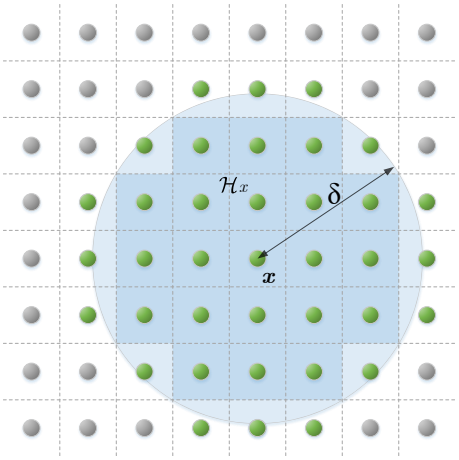

FIGURE 1 Distribution of material points and the integral domain of point $\boldsymbol{X}$

In the bond-based peridynamic modelling framework[4], a solid occupying the domain Ω is discretized by a finite number of material points. A pair of points located within the same horizon are connected to each other via a bond. The resultant force density $\int_{\mathcal{H}_x} \boldsymbol{f}(\boldsymbol{x},t)\,\mathrm{d}V_{x'}$ acting at a material point $\boldsymbol{x}$ is computed as the net force density arising from the connections of all neighboring points within its horizon $\mathcal{H}_x$.

Consider two material points in the same horizon and initially with the respective locations $\boldsymbol{x}$ and $\boldsymbol{x}'$, to give a relative position vector as

$$\boldsymbol{\xi} = \boldsymbol{x}' - \boldsymbol{x}. \tag{2}$$

Assume that at instant t, these two points have been displaced by $\boldsymbol{u}(\boldsymbol{x},t)$ and $\boldsymbol{u}\left(\boldsymbol{x}',t\right)$, respectively. A relative displacement vector can thus be defined as

$$\boldsymbol{\eta} = \boldsymbol{u}\left(\boldsymbol{x}',t\right) - \boldsymbol{u}(\boldsymbol{x},t). \tag{3}$$

In the linearly elastic phase, the local force related function can be formulated as

$$\boldsymbol{f}(\boldsymbol{\eta},\boldsymbol{\xi},t) = \boldsymbol{C}\cdot\boldsymbol{\eta} \tag{4}$$

where $\boldsymbol{C}$ denotes the second-order bond stiffness tensor. Referring to[22], a local shear deformation mechanism is incorporated in addition to the standard stretching mode, to give

$$\boldsymbol{C} = \frac{1}{\xi}\left[c\boldsymbol{n}\otimes\boldsymbol{n} + \kappa\left(\boldsymbol{I} - \boldsymbol{n}\otimes\boldsymbol{n}\right)\right], \tag{5}$$

where $\boldsymbol{n} = \boldsymbol{\xi}/\xi$ is the unit vector in bond direction, with $\xi = \|\boldsymbol{\xi}\|$. The tensor product operator is denoted as $\otimes$, and $\boldsymbol{I}$ denotes the second order identity tensor.

The bond stiffness moduli in the stretch and shear directions are denoted respectively as c and κ (see Figure 2). For an isotropic linear elastic material, these moduli are related to the Young's modulus E and Poisson's ratio ν of the solid body[22]. Specifically, in 3D,

$$c = \frac{6E}{\pi\delta^4(1-2\nu)},\ \kappa = \frac{6E(1-4\nu)}{\pi\delta^4(1+\nu)(1-2\nu)} \tag{6}$$

In 2D, the moduli are obtained as

$$c = \frac{6E}{\pi\delta^3(1-\nu)},\ \kappa = \frac{6E(1-3\nu)}{\pi\delta^3(1-\nu^2)} \tag{7}$$

for plane stress condition, and

$$c = \frac{6E}{\pi\delta^3(1+\nu)(1-2\nu)},\ \kappa = \frac{6E(1-4\nu)}{\pi\delta^3(1+\nu)(1-2\nu)} \tag{8}$$

for plane strain condition.

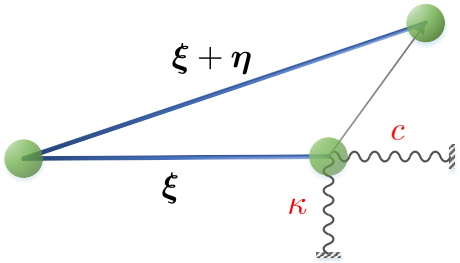

FIGURE 2 Schematic diagram of axial and tangential stiffness

To ensure the numerical calculation accuracy of the peridynamic model, an improved algorithm is adopted to correct the calculation of integral areas. The family of $\boldsymbol{x}$ is extended to include all points with a nonzero overlapping area with the horizon of $\boldsymbol{x}$ and is defined as

$$\mathcal{J}_X(\boldsymbol{x}) = \{\boldsymbol{x} \in \mathbf{R} : C_x \cap \mathcal{H}_x \neq \emptyset\} \tag{9}$$

where C_x denotes the volume one particle cell occupies. That is to say, if any corner of the particle cell belongs to the horizon of particle $\boldsymbol{x}_i$, there exist the interaction forces between the two particles. As shown in Figure 1, the integral area of each particle can be regarded as the overlapping area between the central particle's horizon and the other particle's cell. The correction factor of the integral area can be approximated by

$$P_i^j = \begin{cases} \mathrm{d}x \cdot \mathrm{d}y, & \text{if } C_{x_j} \subset \mathcal{H}_{x_i} \\ \dfrac{\frac{1}{2}\Delta x + \delta - \xi}{\Delta x}, & \text{if } C_{x_j} \not\subset \mathcal{H}_{x_i} \text{ and } C_{x_j} \cap \mathcal{H}_{x_i} \neq \emptyset \\ 0, & \text{if } C_{x_j} \cap \mathcal{H}_{x_i} = \emptyset. \end{cases} \tag{10}$$

where Δx denotes the mesh size.

2.2 | Strain based decomposition of local deformation

The relative displacement vector $\boldsymbol{\eta}$ can be decomposed into normal and tangential components, respectively given as

$$\ell = \frac{1}{\xi}\boldsymbol{\eta} \cdot \boldsymbol{n}, \tag{11}$$

and

$$\boldsymbol{\gamma} = \frac{1}{\xi}(\boldsymbol{\eta} - (\boldsymbol{\eta} \cdot \boldsymbol{n})\boldsymbol{n}). \tag{12}$$

According to[23,55], the relative displacement vector $\boldsymbol{\eta}$ is also linearly related to the local strain tensor $\boldsymbol{\varepsilon}$ and rotation tensor $\boldsymbol{\omega}$:

$$\boldsymbol{\eta} = \boldsymbol{\varepsilon} \cdot \boldsymbol{\xi} - \boldsymbol{\omega} \cdot \boldsymbol{\xi}. \tag{13}$$

Since the rigid body rotation does not contribute to the internal force, the rotation term needs to be eliminated from the displacements vector[23]. Thus we obtain

$$\boldsymbol{\eta} = \boldsymbol{\varepsilon} \cdot \boldsymbol{\xi}. \tag{14}$$

Here, the relative displacement $\boldsymbol{\eta}$ can be physically interpreted as a local deformation vector. Accordingly, the normal and tangential components ℓ and $\boldsymbol{\gamma}$ can also be written in terms of the local strain tensor as

$$\ell = \boldsymbol{n} \cdot \boldsymbol{\varepsilon} \cdot \boldsymbol{n}, \tag{15}$$

$$\boldsymbol{\gamma} = \boldsymbol{n} \cdot \boldsymbol{\varepsilon} \cdot (\boldsymbol{I} - \boldsymbol{n} \otimes \boldsymbol{n}). \tag{16}$$

2.3 | Approximation of strain field

According to[23], the bond strain can be approximated using the displacements of material points surrounding the bond, as illustrated in Figure 3. This bond strain will later be used for introducing plasticity behavior into the force density - strain constitutive relations, as well as incorporation into the bond breakage criteria.

From the discrete displacements of material points, the displacement field in a small volume (named voxel) can be approximated as a multivariate linear function $\hat{\boldsymbol{u}}(\boldsymbol{x})$

$$\hat{\boldsymbol{u}} = \boldsymbol{m} \cdot \boldsymbol{x} + \boldsymbol{c}, \quad \hat{u}_i = m_{ij} x_j + c_i, \quad i, j = 1, 2, 3 \tag{17}$$

where the Einstein summation convention is applied for simplicity, $\boldsymbol{m}$ representing a combination coefficient matrix. The term $\boldsymbol{c}$ denotes the translation of solid body.

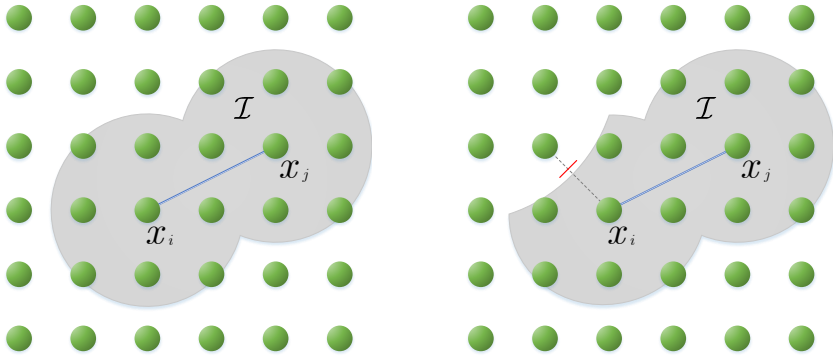

(a) Initial state (b) After a neighboing bond breaks

FIGURE 3 Approximate area of a bond connecting two material points

To achieve sufficient accuracy of the approximation, while retaining computational efficiency, the voxel should include a suitable number of material points. The approximation of displacement field $\hat{\boldsymbol{u}}$ will be based on material points with position vector $\boldsymbol{x}$ that satisfy the following

$$\mathcal{I}_x(\boldsymbol{x}) = \{\boldsymbol{x} \in \boldsymbol{R} : \|\boldsymbol{x} - \boldsymbol{x}_i\| \leq r\Delta x \ \cup \ \|\boldsymbol{x} - \boldsymbol{x}_j\| \leq r\Delta x\} \tag{18}$$

where Δx is the spacing in a uniform grid and r denoting the size of approximation domain. For small deformation problems considered in this paper, it is found that the size of approximation domain r in (18) does not influence the results significantly. An example will be provided later in Section 7.1.1.

As illustrated in Figure 3, the material points used to fit the bond displacement function are chosen from the neighboring points of the two connecting points. Note that when the bond connecting the two neighboring material points is broken, these two points will no longer be part of each other's active neighborhood.

Focusing on infinitesimal deformation in this paper, the strain in the voxel can be obtained as:

$$\varepsilon_{ij} = \frac{1}{2}\left(\frac{\partial \hat{u}_i}{\partial x_j} + \frac{\partial \hat{u}_j}{\partial x_i}\right) \tag{19}$$

Combining Equation (17) and Equation (19) establishes the connection between local strain $\boldsymbol{\varepsilon}$ and the coefficient matrix $\boldsymbol{m}$:

$$\varepsilon_{ij} = \frac{1}{2}(m_{ij} + m_{ji}) \tag{20}$$

For ease of implementation, the coefficient matrix $\boldsymbol{m}$ and the translation term $\boldsymbol{c}$ can be combined into a new matrix:

$$\boldsymbol{M} = \begin{bmatrix} m_{11} & m_{21} & m_{31} \\ m_{12} & m_{22} & m_{32} \\ m_{13} & m_{23} & m_{33} \\ c_1 & c_2 & c_3 \end{bmatrix} \tag{21}$$

In addition, we define a matrix $\boldsymbol{U}$ comprising the displacement components of all n material points within $\mathcal{I}_x$:

$$\boldsymbol{U} = \begin{bmatrix} u_{(1)1} & u_{(1)2} & u_{(1)3} \\ u_{(2)1} & u_{(2)2} & u_{(2)3} \\ \vdots & \vdots & \vdots \\ u_{(n)1} & u_{(n)2} & u_{(n)3} \end{bmatrix} \tag{22}$$

A location matrix $\boldsymbol{X}$ collates the location information of all material points in $\mathcal{I}_x$:

$$\boldsymbol{X} = \begin{bmatrix} x_{(1)1} & x_{(1)2} & x_{(1)3} & 1 \\ x_{(2)1} & x_{(2)2} & x_{(2)3} & 1 \\ \vdots & \vdots & \vdots & \vdots \\ x_{(n)1} & x_{(n)2} & x_{(n)3} & 1 \end{bmatrix} \tag{23}$$

By applying the least square method and minimizing the sum of residuals in terms of each displacement component[23], we obtain the following relationship

$$\boldsymbol{M} = \boldsymbol{T}\boldsymbol{U} \tag{24}$$

where

$$\boldsymbol{T} = (\boldsymbol{X}^T\boldsymbol{X})^{-1}\boldsymbol{X}^T \tag{25}$$

2.4 | Bond moduli across interface

For rock or concrete materials that usually contain a variety of soft and hard inclusions, the micro moduli of bonds across material interface (as illustrated in Figure 4) can be estimated according to a homogenization method. Assume that the bond

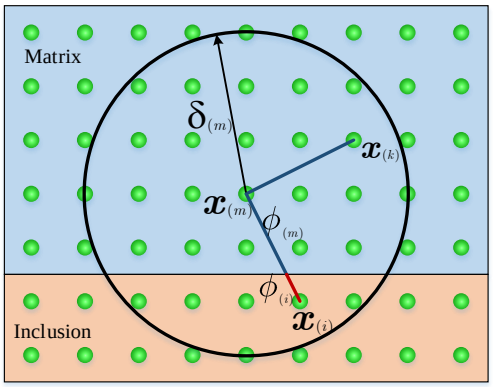

FIGURE 4 Illustration of bonds across an interface which separates two different materials

stretch and shear moduli for the matrix phase are denoted by $c_{(m)}$ and $\kappa_{(m)}$, and the respective variables for inclusions are $c_{(i)}$ and $\kappa_{(i)}$. In addition, for each bond cross an interface, the length-related fractions in the matrix and inclusion are denoted by $\phi_{(m)}$ and $\phi_{(i)}$. The effective stiffness moduli are then estimated as

$$c_{eff} = c_{(m)}c_{(i)}\frac{\phi_{(m)} + \phi_{(i)}}{c_{(i)}\phi_{(m)} + c_{(m)}\phi_{(i)}}, \qquad \kappa_{eff} = \kappa_{(m)}\kappa_{(i)}\frac{\phi_{(m)} + \phi_{(i)}}{\kappa_{(i)}\phi_{(m)} + \kappa_{(m)}\phi_{(i)}} \tag{26}$$

In benchmark study 7.1.2, a bi-material plate with a crack is considered to study the crack-inclusion interactions.

3 | BOND BREAKAGE CONSIDERING SHEAR DEFORMATION

For describing bond failure, a characteristic function $\mu(\boldsymbol{u}, \boldsymbol{\xi})$ is introduced into the force–relative displacement relation.

$$\boldsymbol{f}(\boldsymbol{u}, \boldsymbol{\xi}) = \mu(\boldsymbol{u}, \boldsymbol{\xi})(c\ell\boldsymbol{n} + \kappa\boldsymbol{\gamma}) \tag{27}$$

According to[1], the local damage variable $d(\boldsymbol{x})$ at point $\boldsymbol{x}$ is defined in the form

$$d(\boldsymbol{x}) = 1 - \frac{\int_{H_x} \mu(\boldsymbol{\eta}, \boldsymbol{\xi}) \mathrm{d}V_{x'}}{\int_{H_x} \mathrm{d}V_{x'}} \tag{28}$$

with

$$\mu(\boldsymbol{u}, \boldsymbol{\xi}) = \begin{cases} 1, \text{ if } \ell < \ell_c \text{ and } \|\boldsymbol{\gamma}\| < \gamma_c \\ 0, \text{ if } \ell \geq \ell_c \text{ or } \|\boldsymbol{\gamma}\| > \gamma_c \end{cases} \tag{29}$$

where ℓ_c and γ_c are the critical values of the bond stretch and bond rotation, respectively. In the XPD framework, the tangential stiffness is introduced in addition to the normal stiffness in classical BB-PD, as illustrated in Figure 2. Conceptually, the pair of material points can be understood as being connected by two bonds, to respectively govern the normal deformation and shear deformation between the points. Thus the stored energy of the normal bond and tangential bond can be obtained as:

$$G_c = \int_0^{\delta} \int_z^{\delta} \int_0^{2\pi} \int_0^{\cos^{-1}(z/\xi)} (\frac{1}{2} c \ell^2 \xi) \xi^2 \sin\theta \mathrm{d}\theta \mathrm{d}\phi \mathrm{d}\xi \mathrm{d}z \tag{30}$$

$$G_s = \int_0^{\delta} \int_z^{\delta} \int_0^{2\pi} \int_0^{\cos^{-1}(z/\xi)} (\frac{1}{2} \kappa \gamma^2 \xi) \xi^2 \sin\theta \mathrm{d}\theta \mathrm{d}\phi \mathrm{d}\xi \mathrm{d}z \tag{31}$$

Solving the integral equation yields the critical value of bond stretch and bond shear deformation:

$$\ell_c = \sqrt{\frac{10G_c}{\pi\delta^5 c}}, \qquad \gamma_c = \sqrt{\frac{10G_s}{\pi\delta^5 \kappa}} \tag{32}$$

Substituting the material micromodulus in (6), we obtain

$$\ell_c = \sqrt{\frac{5G_c(1-2\nu)}{3E\delta}}, \qquad \gamma_c = \sqrt{\frac{5G_s(1+\nu)(1-2\nu)}{3E\delta(1-4\nu)}} \tag{33}$$

For two-dimensional cases,

$$G_c = 2h \int_0^{\delta} \int_z^{\delta} \int_0^{\cos^{-1}(z/\xi)} (\frac{1}{2} c \ell^2 \xi) \xi \mathrm{d}\phi \mathrm{d}\xi \mathrm{d}z \tag{34}$$

$$G_s = 2h \int_0^{\delta} \int_z^{\delta} \int_0^{\cos^{-1}(z/\xi)} (\frac{1}{2} \kappa \gamma^2 \xi) \xi \mathrm{d}\phi \mathrm{d}\xi \mathrm{d}z \tag{35}$$

The critical bond stretch and bond shear deformation becomes:

$$\ell_c = \sqrt{\frac{4G_c}{h\delta^4 c}}, \quad \gamma_c = \sqrt{\frac{4G_s}{h\delta^4 \kappa}} \tag{36}$$

The specific value depends on the type of plane problem.

In this paper, $\boldsymbol{\gamma}$ is determined from the bond strain instead of the relative rotation angle, in order to eliminate the effect of rigid body rotation as discussed in Section 2.2.

In some tests, it is not enough to only consider the tensile fracture of a bond, as done in a standard peridynamic model. The introduction of critical shear deformation helps to capture the shear crack observed in experimental tests. This will be shown later in benchmark study 7.1.3.

4 | ELASTOPLASTIC FORMULATION OF THE CONSTITUTIVE MODEL

We now proceed to extend the above peridynamic formulation by taking into account plastic deformation, following the standard strain decomposition below

$$\boldsymbol{\varepsilon} = \boldsymbol{\varepsilon}^e + \boldsymbol{\varepsilon}^p \tag{37}$$

In view of Equation (13), the local deformation vector can also be decomposed into elastic $\boldsymbol{\eta}^e = \boldsymbol{\varepsilon}^e \cdot \boldsymbol{\xi}$ and plastic components $\boldsymbol{\eta}^p = \boldsymbol{\varepsilon}^p \cdot \boldsymbol{\xi}$,

$$\boldsymbol{\eta} = (\boldsymbol{\varepsilon}^e + \boldsymbol{\varepsilon}^p) \cdot \boldsymbol{\xi} = \boldsymbol{\eta}^e + \boldsymbol{\eta}^p \tag{38}$$

The local force density function can thus be reformulated as

$$\boldsymbol{f} = \boldsymbol{C} \cdot (\boldsymbol{\eta} - \boldsymbol{\eta}^p) \tag{39}$$

or equivalently

$$\boldsymbol{f} = c(\ell - \ell^p)\boldsymbol{n} + \kappa(\boldsymbol{\gamma} - \boldsymbol{\gamma}^p) \tag{40}$$

with $\ell^p = \boldsymbol{n} \cdot \boldsymbol{\varepsilon}^p \cdot \boldsymbol{n}$ and $\boldsymbol{\gamma}^p = \boldsymbol{n} \cdot \boldsymbol{\varepsilon}^p \cdot (\boldsymbol{I} - \boldsymbol{n} \otimes \boldsymbol{n})$.

The total bond stretch ℓ and the local strain $\boldsymbol{\varepsilon}$ can be written in terms of the displacement field $\boldsymbol{u}$ that was determined earlier. We thus replace the expression $\boldsymbol{f}(\boldsymbol{\eta}, \boldsymbol{\xi}, t)$ by $\boldsymbol{f}(\boldsymbol{u}, \boldsymbol{\xi}, t)$. For numerical implementation, the force density - strain relation is rewritten as

$$\boldsymbol{f}(\boldsymbol{u}, \boldsymbol{\xi}, t) = c(\ell - \boldsymbol{n} \cdot \boldsymbol{\varepsilon}^p \cdot \boldsymbol{n})\boldsymbol{n} + \kappa \boldsymbol{n} \cdot (\boldsymbol{\varepsilon} - \boldsymbol{\varepsilon}^p) \cdot (\boldsymbol{I} - \boldsymbol{n} \otimes \boldsymbol{n}) \tag{41}$$

The key step is thus to determine the plastic component $\boldsymbol{\varepsilon}^p$, which can be obtained following the standard solution strategy for classical plasticity models. For better clarity in this paper, two commonly used constitutive models are considered.

A Drucker-Prager yield function with isotropic hardening is provided:

$$\phi = \sqrt{J_2} + \alpha I_1 - k(\gamma_p) \tag{42}$$

where $J_2 = \frac{1}{2} S_{ij} S_{ij}$ is the second invariant of deviator stress, which is in turn defined as $S_{ij} = \sigma_{ij} - \frac{1}{3}\sigma_{kk}\delta_{ij}$. $I = \sigma_{kk}$ is the first invariant of the stress tensor, $\boldsymbol{\sigma} = \mathbb{C} : (\boldsymbol{\varepsilon} - \boldsymbol{\varepsilon}^p)$ with $\mathbb{C}$ being the initial elastic stiffness tensor and $\boldsymbol{\varepsilon}$ the total strain approximated locally. α is a material constant and $k(\gamma_p)$ is the hardening function. In this study, we take the following form

$$k(\gamma_p) = k_0 + \tau_c(1 - \exp(-w\gamma_p)), \tag{43}$$

where k_0 is the initial threshold, while τ_c denotes the maximum expansion to yield surface due to plastic hardening; w is the parameter controlling the hardening rate. Here defines $e^p_{ij} = \varepsilon^p_{ij} - \delta_{ij}\frac{\varepsilon^p_{kk}}{3}$,

$$\gamma_p = \int \sqrt{\frac{2}{3} \mathrm{d}e^p_{ij} \mathrm{d}e^p_{ij}} \tag{44}$$

The parameter α and k_0 can be related to the material cohesion c_0 and friction angle φ such that

$$\alpha = \frac{\sin\varphi}{\sqrt{3}}, \quad k_0 = \frac{2c_0\cos\varphi}{\sqrt{3}} \tag{45}$$

The structural complexity plays an important role in determine the mechanical property of geomaterials. To replicate plastic deformation and crack growth of materials with anisotropy, we also introduce an oriented yield function

$$\phi = ||\tau|| + \alpha\sigma_n - k_0 \tag{46}$$

where σ_n denotes the stress corresponding to the preferential direction $\boldsymbol{n}_y$, α determine the degree of anisotropy, and $||\tau||$ denotes the stress perpendicular to $\boldsymbol{n}_y$; k_0 is a material constant which defines the elastic domain.

For simplicity in this paper, we adopt an associated flow rule for plastic evolution.

5 | ELASTOPLASTIC FRACTURE

For the solution of the elastoplastic fracture problems, the following bond constitutive relation is adopted:

$$\boldsymbol{f}(\boldsymbol{u}, \boldsymbol{\xi}) = \mu(\boldsymbol{u}, \boldsymbol{\xi})(c(\ell - \ell^p)\boldsymbol{n} + \kappa(\boldsymbol{\gamma} - \boldsymbol{\gamma}^p)) \tag{47}$$

where ℓ^p and $\boldsymbol{\gamma}^p$ are the plastic parts of stretch and shear deformation, respectively.

Following similar concept in [56,57,58] where the fracture is driven by the elastic strain energy and the stored plastic energy, we adopted an energy-based criterion for the elasto-plasticity-fracture coupling. The tensile and shear components of the elastic local strain energy contributing to bond breakage are:

$$w^e_n(\boldsymbol{\xi}) = \frac{1}{2} r_e(\boldsymbol{\xi}) c(\ell^e)^2 \xi \tag{48}$$

$$w_s^e(\boldsymbol{\xi}) = \frac{1}{2}\kappa \boldsymbol{\gamma}^e \cdot \boldsymbol{\gamma}^e \xi \tag{49}$$

where r_e is used to distinguish between the anisotropic effect of bond stretch and compression on fracture:

$$r_e = \begin{cases} 1, \text{ if } \ell^e > 0 \\ 0, \text{ if } \ell^e \leqslant 0 \end{cases} \tag{50}$$

The plastic component of stored energy is obtained as the sum of increment value over the entire loading history:

$$\dot{w}_n^p(\boldsymbol{\xi}) = (1-\beta) f_n \dot{\ell}^p \xi \tag{51}$$

$$\dot{w}_s^p(\boldsymbol{\xi}) = (1-\beta) \boldsymbol{f}_s \cdot \dot{\boldsymbol{\gamma}}^p \xi \tag{52}$$

where $f_n = c\ell^e$ and $\boldsymbol{f}_s = \kappa \boldsymbol{\gamma}^e$, Parameter β denotes the fraction of plastic work dissipated through heating[56,57]. Because calibrating this parameter is difficult and necessitates specific tests, most approaches just assume a constant value[59,58]. Here, we assume that the energy stored from compressive flow does not contribute to the fracture process, via a plasticity coefficient r_p:

$$r_p = \begin{cases} 1, \text{ if } \ell^p > 0 \\ 0, \text{ if } \ell^p \leqslant 0 \end{cases} \tag{53}$$

Hence, the plastic energy in normal direction driving the bond breakage can be expressed as

$$w_n^p(\boldsymbol{\xi}) = r_p(\boldsymbol{\xi}) w_n^p(\boldsymbol{\xi}) \tag{54}$$

Finally, the energy required to break all bonds per unit fracture area can be determined as:

$$G_c = \int_0^\delta \int_z^\delta \int_0^{2\pi} \int_0^{\cos^{-1}(z/\xi)} (w_n^e(\boldsymbol{\xi}) + w_n^p(\boldsymbol{\xi}))\xi^2 \sin\theta \mathrm{d}\theta \mathrm{d}\phi \mathrm{d}\xi \mathrm{d}z \tag{55}$$

$$G_s = \int_0^\delta \int_z^\delta \int_0^{2\pi} \int_0^{\cos^{-1}(z/\xi)} (w_s^e(\boldsymbol{\xi}) + w_s^p(\boldsymbol{\xi}))\xi^2 \sin\theta \mathrm{d}\theta \mathrm{d}\phi \mathrm{d}\xi \mathrm{d}z \tag{56}$$

We define two scalar functions calculated from the bond strain loading history:

$$Y_1(\boldsymbol{\xi}) = (w_n^e(\boldsymbol{\xi}) + w_n^p(\boldsymbol{\xi}))/\xi, \quad Y_2(\boldsymbol{\xi}) = (w_s^e(\boldsymbol{\xi}) + w_s^p(\boldsymbol{\xi}))/\xi \tag{57}$$

Solving the integral equation yields the critical value of $Y(\boldsymbol{\xi})$:

$$Y_c = \frac{5G_c}{\pi\delta^5}, \quad Y_s = \frac{5G_s}{\pi\delta^5} \tag{58}$$

Similarly, for two-dimensional models,

$$G_c = 2h \int_0^\delta \int_z^\delta \int_0^{\cos^{-1}(z/\xi)} (w_n^p(\boldsymbol{\xi}) + w_n^p(\boldsymbol{\xi}))\xi \mathrm{d}\phi \mathrm{d}\xi \mathrm{d}z \tag{59}$$

$$G_s = 2h \int_0^\delta \int_z^\delta \int_0^{\cos^{-1}(z/\xi)} (w_s^p(\boldsymbol{\xi}) + w_s^p(\boldsymbol{\xi}))\xi \mathrm{d}\phi \mathrm{d}\xi \mathrm{d}z \tag{60}$$

Solving for the integral gives

$$Y_c = \frac{2G_c}{h\delta^4}, \quad Y_s = \frac{2G_s}{h\delta^4} \tag{61}$$

For any loading step, a bond is taken to be broken if $Y_1(\boldsymbol{\xi}) > Y_c$ or $Y_2(\boldsymbol{\xi}) > Y_s$ and removed from the structure.

6 | NUMERICAL IMPLEMENTATION

6.1 | Quasi-static problems

The integration form of the static equilibrium equation is given as:

$$\int_{\mathcal{H}_x} \boldsymbol{f}(\boldsymbol{u}, \boldsymbol{\xi}) \mathrm{d}V_{x'} + \boldsymbol{b}(\boldsymbol{x}) = 0 \tag{62}$$

In the discretized form for peridynamic, this becomes

$$\sum_{l=1}^{N_{\mathcal{H}_{(k)}}} \boldsymbol{f}_{(k)(l)} V_{(l)} + \boldsymbol{b}_{(k)} = 0 \tag{63}$$

where subscript (k) denote the material point at $x_{(k)}$, the subscripts of $\boldsymbol{f}$ indicating the two connected points, $N_{\mathcal{H}_{(k)}}$ represents the number of material points in the horizon connected to point $x_{(k)}$, and $V_{(l)}$ represents the volume occupied by point $\boldsymbol{x}_{(l)}$.

The resulting force balance equation is thus,

$$\sum_{l=1}^{N_{\mathcal{H}_{(k)}}} \boldsymbol{f}_{(k)(l)} V_{(l)} V_{(k)} + \boldsymbol{b}_{(k)} V_{(k)} = 0 \tag{64}$$

For quasi-static problems, the solution strategy for elastic fracture models is summarized in Algorithm 1. For the maximum

Algorithm 1 The elastic solution of XPDM fracture

Input: Given loading step $n = 0$, $\boldsymbol{U}_0$
Solve: $\boldsymbol{U} = -\boldsymbol{K} \setminus [\boldsymbol{F}_{int}(\boldsymbol{U}_n) - \boldsymbol{F}_{ext}]$
Output: output result

1: **if** any PD bond is broken **then**
2: Update $\boldsymbol{K}$
3: Return to **Solve**
4: **else**
5: $n = n + 1$
6: $\boldsymbol{U}_n = \boldsymbol{U}_{n-1} + \Delta \boldsymbol{u}_n$
7: **end if**

number of bonds allowed to break at each equilibrium step, we refer to[60] for a detailed analysis of static fracture problems. A similar analysis is carried out for the examples in Subsections 7.1 and 7.3. When the number of broken bonds allowed per step is less than or equal to 4, the difference is marginal in terms of fracture propagation direction and macroscopic material strength. In general, the more fracture bonds allowed per step, the more efficient the corresponding computation will be. For the static problems in this manuscript, the number of broken bonds allowed per step is set at 4.

6.2 | Dynamic problems

An explicit time integration approach below is adopted for dynamic problems,

$$\dot{\boldsymbol{u}}^{n+\frac{1}{2}} = \dot{\boldsymbol{u}}^{n} + \frac{\Delta t}{2} \ddot{\boldsymbol{u}}^{n}, \tag{65}$$

$$\boldsymbol{u}^{n+1} = \boldsymbol{u}^{n} + \Delta t \dot{\boldsymbol{u}}^{n+\frac{1}{2}} \tag{66}$$

where $\dot{\boldsymbol{u}}$ is the velocity vector and $\ddot{\boldsymbol{u}}$ is the acceleration vector. To ensure numerical stability, the time step Δt is limited by

$$\Delta t \leq \frac{\Delta_{min}}{c_k}, \tag{67}$$

$$c_k = \sqrt{K/\rho} \tag{68}$$

where Δ_{min} is the minimum nodal distance in the discretized domain, K is the bulk modulus and ρ is the mass density. With the force-displacement relations of the system

$$\boldsymbol{F} = \boldsymbol{K}\boldsymbol{u}, \tag{69}$$

$$\ddot{\boldsymbol{u}} = \frac{\boldsymbol{F}}{m} \tag{70}$$

m represents the material point mass which is the same for each material point under uniform grids.

The dynamic solutions can be obtained correspondingly. From the material point displacements obtained from the previous time step, new broken bonds may develop. The lists of neighboring points are then updated, as well as the corresponding stiffness matrix $\boldsymbol{K}$.

6.3 | Elastoplastic response

In a uniform distributed material point system, the representative volume of each point is denoted by V_p. According to Equation (41), the force in each bond can be computed as

$$\mathbf{f}_{bond} = V_k V_l[(c\ell\boldsymbol{n} - \boldsymbol{n}\cdot\boldsymbol{\varepsilon}^p\cdot\boldsymbol{n})\boldsymbol{n} + \kappa\boldsymbol{n}\cdot(\boldsymbol{\varepsilon}-\boldsymbol{\varepsilon}^p)\cdot(\boldsymbol{I}-\boldsymbol{n}\otimes\boldsymbol{n})] \tag{71}$$

The internal force caused by the extended peridynamic bond can be re-written as:

$$\mathbf{f}_{bond} = \mathbf{f} - \mathbf{f}_{pla}, \tag{72}$$

where $\mathbf{f} = V_k V_l^2[c\ell\boldsymbol{n} + \kappa\boldsymbol{n}\cdot\boldsymbol{\varepsilon}\cdot(\boldsymbol{I}-\boldsymbol{n}\otimes\boldsymbol{n})]$ and $\mathbf{f}_{pla} = V_k V_l(C\cdot\boldsymbol{\varepsilon}^p\cdot\boldsymbol{\xi})$,

The global internal force vector $\boldsymbol{F}_{int}$ can be obtained from the assembly bond force vectors $\mathbf{f}_{bond}$,

$$\boldsymbol{F}_{int} = \boldsymbol{F} - \boldsymbol{F}_{pla} \tag{73}$$

Referring to[23], the assembly of $\boldsymbol{F}$ can be done via a matrix operation:

$$\boldsymbol{F} = \boldsymbol{K}\boldsymbol{U} \tag{74}$$

where $\boldsymbol{K}$ is the global stiffness matrix of the peridynamic region and $\boldsymbol{U}$ is the global displacement vector.

From Equations (17) and (20) in subsection 2.3, the bond strain can be determined from the displacements of local area. The global strain - displacement relations can be thus written as:

$$\boldsymbol{E} = \boldsymbol{K}_{u\to\varepsilon}\boldsymbol{U} \tag{75}$$

Here $\boldsymbol{K}_{u\to\varepsilon}$ represents the strain - displacement transformation matrix, and $\boldsymbol{E}$ is a global strain vector containing all bond strains. Once the bond strain is determined, the corresponding plastic strain $\boldsymbol{E}^p$ at each increment can be calculated through the elastoplastic constitutive relationship.

According to Equations (4) and (14), the bond force of each bond can be directly obtained from the bond strain. The relation between the global strain column vector and the global nodal force vector can be expressed as

$$\boldsymbol{F} = \boldsymbol{K}_{\varepsilon\to f}\boldsymbol{E} \tag{76}$$

where $\boldsymbol{K}_{\varepsilon\to f}$ represents the force - strain transformation matrix.

In view of $\boldsymbol{f}_{pla} = V_k V_l(C\cdot\boldsymbol{\varepsilon}^p\cdot\boldsymbol{\xi})$, the global force vector $\boldsymbol{F}_{pla}$ in Equation (73) can be written as

$$\boldsymbol{F}_{pla} = \boldsymbol{K}_{\varepsilon\to f}\boldsymbol{E}^p \tag{77}$$

Given an increasing external force, new broken bonds developed constantly. The corresponding list of active neighboring material points is required to be updated, and the contribution of a new broken bond has to be removed. The structure is modified accordingly with reduced stiffness, until the failure of the next bond.

Similar to the incremental nonlinear finite element scheme[61], the Newton-Raphson scheme for the solution of the incremental nonlinear equations can be implemented in the elastoplastic XPDM framework. The pseudo-code format of the nonlinear framework is summarised in Algorithm 5.

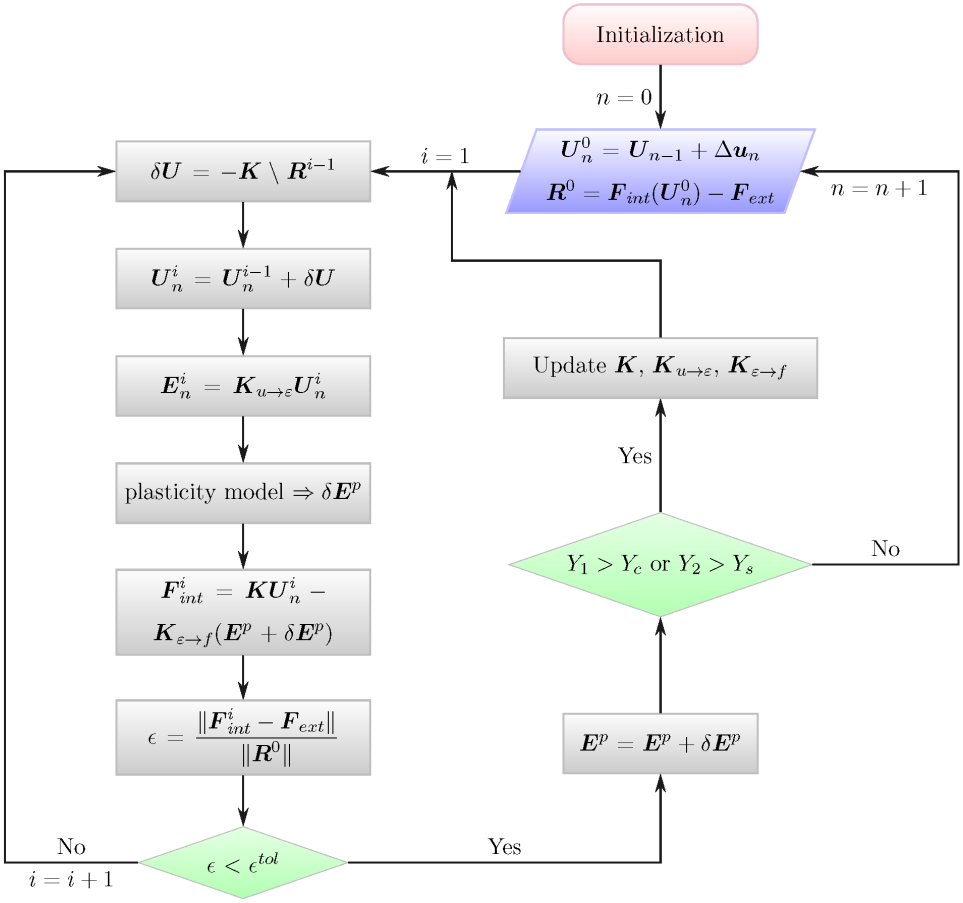

FIGURE 5 The elastoplastic XPDM iterative scheme

6.4 | FEM/XPDM coupling implementation

The solution of a typical nonlinear mechanical problem usually involves the Newton-Raphson iterative scheme, which can be computationally expensive, especially for peridynamic models due to their nonlocality. Here, we refer to the solution strategy in multiscale methods, where the modelling resolution is only increased locally at the regions of interest[62,63,64,65,66,67,68,69,60,70,71]. Particularly, we refer to the PD/FEM coupling method proposed by[62], such that the PD method can be practically adopted for large-scale calculations. By restricting the PD models to the interior regions of interest, the difficulty of imposing boundary conditions at the physical boundaries is also circumvented.

An illustration for the XPDM-FEM coupling is provided in Figure 6, where the square meshes represent finite elements, and the discrete green nodes represent peridynamic points. When calculating the forces acting on green nodes, the yellow nodes are taken as XPDM nodes to approximate bond strain and bond stretch[23]; when calculating the forces at yellow nodes, the green nodes are taken as finite element nodes. By following this coupling procedure, boundary conditions and external loads can be imposed easily on the finite element nodes. Computational time is also reduced by limiting the high resolution PD model to the region of interest.

The numerical implementation in the finite element region follows standard procedure[61], with the global internal force vector assembled from the element internal force vectors to give

$$\boldsymbol{F}_{int}^{ele} = \int_{\Omega^{ele}} \boldsymbol{B}^T \boldsymbol{\sigma} \mathrm{d}V, \quad \boldsymbol{\sigma} = \mathbb{C}^0 : (\boldsymbol{\varepsilon} - \boldsymbol{\varepsilon}^p) \tag{78}$$

where $\boldsymbol{B}$ is the strain-displacement matrix.

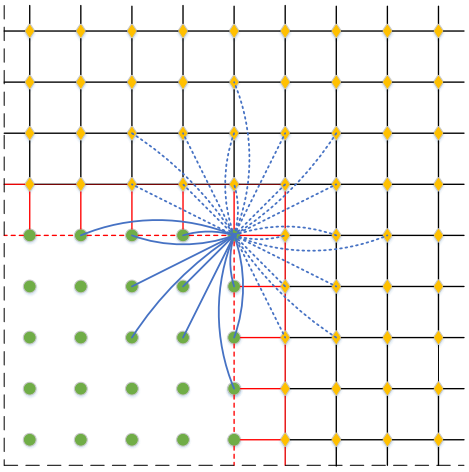

FIGURE 6 The schematic diagram of the FEM/PD coupling method

For the XPDM/FEM coupling scheme adopted, the global internal force of the system in Algorithm 5 is replaced by assembling the internal force of both the finite element and peridynamic regions.

7 | BENCHMARK STUDIES FOR CRACK PROPAGATION

In this section, several benchmark examples are carried out to verify the effectiveness of XPDM in predicting different crack propagations. In the following examples, the structural models are divided into two domains: the region of interest discretized with XPD points (within the dotted line), and the remaining regions discretized using FE mesh. All problems considered assume the plane stress condition unless specifically mentioned.

This section is divided into 3 parts: part 1 in Section 7.1 concerns with quasi-static brittle fracture, part 2 in Section 7.2 addresses dynamic fractures, and part 3 in Section 7.3 discusses on elastoplastic problems. In Section 7.1, the fracture in subsections 7.1.1 is mainly caused by the critical bond stretch. In subsection 7.1.3, we consider fracture processes with significant shear mechanisms, to demonstrate the necessity of the proposed critical shear criteria in capturing the experimental observations.

7.1 | Quai-static brittle fracture

7.1.1 | Koyna dam

This examples presents a practical engineering scenario for the implementation of XPDM. Koyna dam is one of the largest gravity dam located in India, which is analyzed for static solution of crack propagation due to the overflow. The geometry and boundary conditions are shown in Figure 7, where the initial crack is located at the changing slope on the downstream face. The applied loads comprised the self weight, the full reservoir hydrostatic load plus the overflow load with an increasing height. To our knowledge, this is the first attempt in the literature using peridynamics to solve the problem. This problem has been modeled using the XFEM[72] and the improved phase-field model[73,74]. The material properties of the dam are taken from[72]: $E = 25$ GPa, $\nu = 0.2$, $\rho = 2450$ kg/m^3, $\rho_w = 1000$ kg/m^3, $g = 9.8$ m/s^2. For XPD parameters: the horizon is $\delta = 0.375$ m, with a grid spacing that is one-third of it. The critical energy release rate is 60 N/m.

As shown in Figure 8, with the increasing overflow height, a single crack firstly propagates from the predefined notch to the downstream face with a slightly increased inclination. As the crack propagates, the self-weight induced increasing compressive stress along the crack tip, which slows down the fracture speed. A crack branch subsequently occurs and propagates upwards. The crack patterns match well with the prediction in[74]. Additionally, the overflow height versus the horizontal crest displacement is also recorded in Figure 9. Overall, a good agreement is found between our computed responses and the results obtained in literature[73]. Note also that Figure 9 depicts consistent numerical results for two different approximation domain sizes in (18).

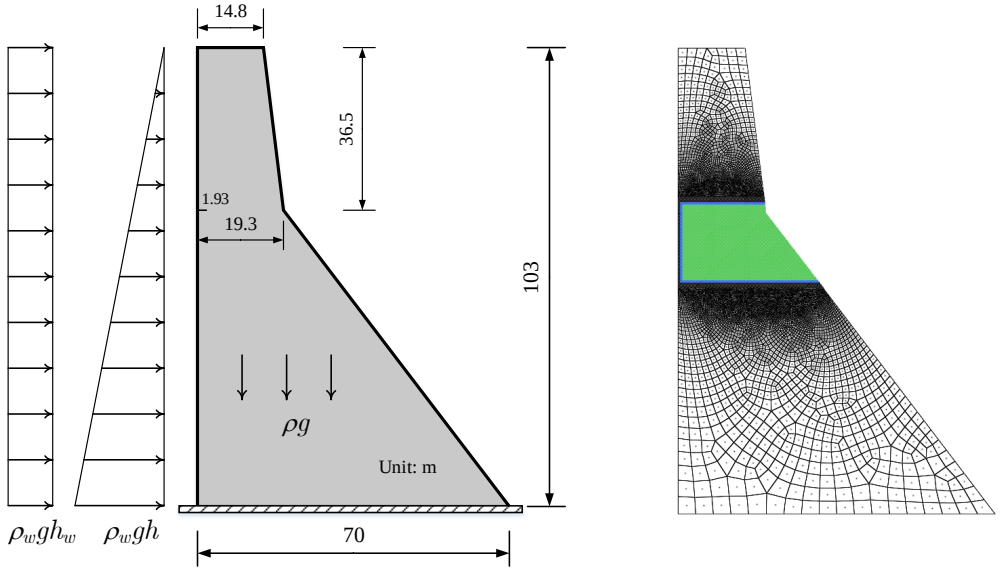

(a) The geometry, boundary and loading conditions

(b) FEM/XPDM discretization

FIGURE 7 Koyna dam

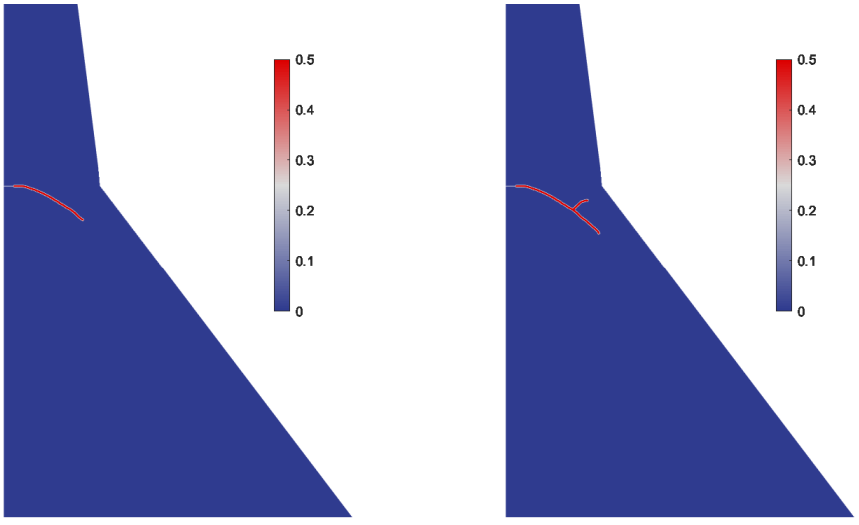

(a) $H_{overflow} = 8.6$m, $U_{crest} = 38.8$mm

(b) $H_{overflow} = 10$m, $U_{crest} = 60.1$mm

FIGURE 8 Koyna dam: crack patterns predicted by XPDM

7.1.2 | Crack deflection due to inclusion

The second example considers a model with inclusions in which the bonds across the interface are determined using homogenization concept, to demonstrate the capability of the proposed model in capturing the effect of soft and hard inclusions on the crack propagation tendency. The geometry and boundary conditions are taken from[75,76]. As shown in Fig. 10, the configuration consists of a rectangular plate with an off-center circular inclusion. The material parameters of the matrix are $E = 6$ GPa, $\nu = 0.2$. Two different ratios of elastic modulus ($E_{inclusion}/E_{mattrix}$) are 10 and 0.1. The PD horizon $\delta = 0.08$ mm, grid spacing $\Delta x = 0.025$ mm and critical energy release rate $G_c = 1000$ N/m.

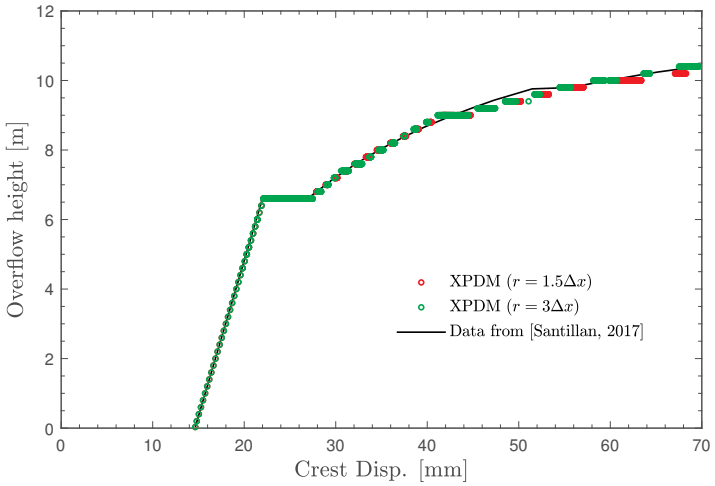

FIGURE 9 Graphs of overflow height versus crest displacement for the Koyna dam

As shown in Fig. 10, the crack growth direction is highly dependent on the type of inclusion. In the case of a rigid inclusion, the crack deflects away from it. Conversely, for a soft inclusion, the crack is attracted towards it. These predictions are consistent with the published results in [77,75,76].

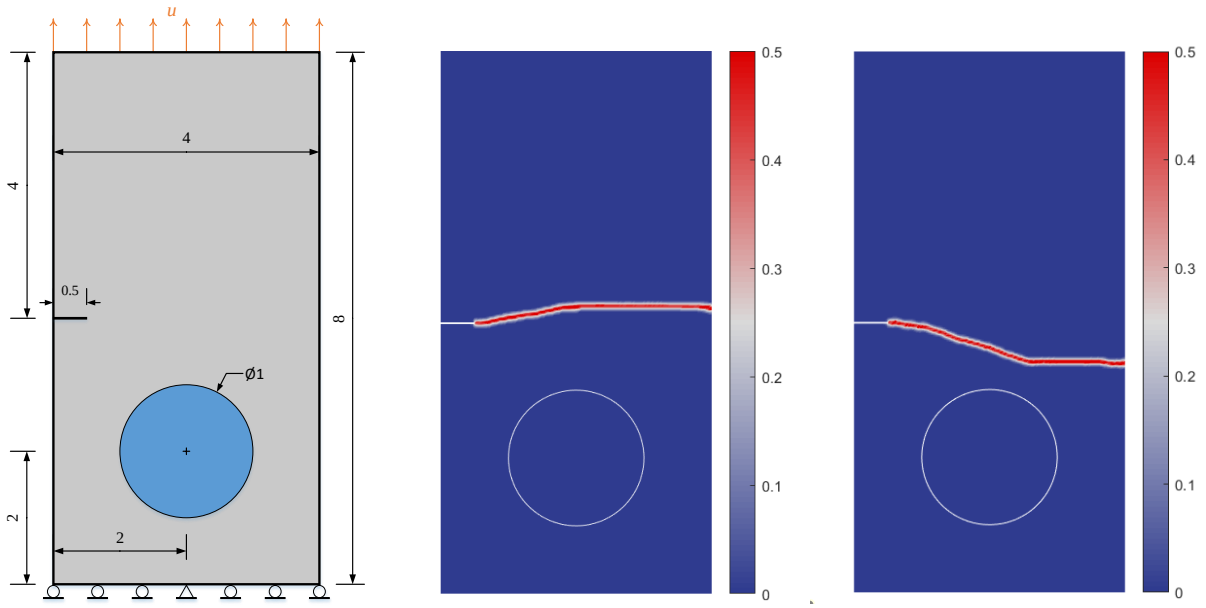

(a) The geometry and boundary conditions (b) Rigid inclusion (c) Soft inclusion

FIGURE 10 Crack deflection due to inclusion

7.1.3 | Compression of a rock specimen with two inclined parallel notches

To demonstrate the capability of XPDM in predicting crack propagation involving fracture coalescence, a specimen containing two parallel pre-cracks subjected to compressive loading is considered here. This problem has been extensively investigated experimentally and numerically employing pre-fractured specimens of gypsum [78,79,80,81,82,83]. The elastic constants of the solid material are $E = 5.96$ GPa, $\nu = 0.2$, with critical energy release rate $G_c = 20$ N/m and critical shear energy release rate $G_s = 100$ N/m. The PD horizon is $\delta = 2$ m and the grid spacing of PD region is $\delta/4$. This example assumes the plane strain condition.

Fig. 11 (a) presents the distribution of two prefabricated cracks in Case 1. The crack patterns observed experimentally, and the numerical results predicted by XPDM considering only critical stretch, are depicted in Figs. 11 (b) and (c) respectively. It is clearly shown that the predicted crack pattern without considering critical shear deformation differs considerably from that observed in the experimental tests. The same problem is also reported in[81] using the phase field methods, when an inadequate shear failure mechanism leads to wrong fracture profiles.

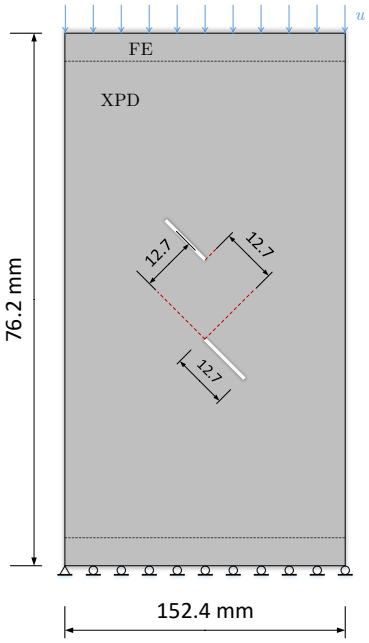

(a) The geometry and boundary conditions

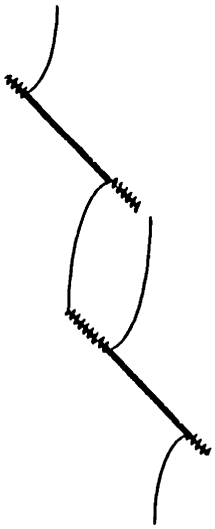

(b) Experimental results

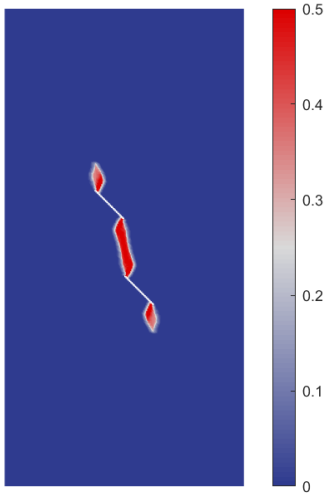

(c) Numerical modeling considering only critical stretch

FIGURE 11 Case 1

With the incorporation of critical shear deformation γ_c in Case 1, the numerical results in Fig. 12 give a crack pattern similar to the experimental observation. Four wing cracks initiate at both the internal and external tips of the pre-existing flaws, before coalescence occurs to connect the inner tip of the lower notch and one wing crack. Finally, two shear cracks appear at the outer tip of two notches.

Fig. 13 (a) shows another specimen with a different distribution of prefabricated cracks (Case 2). The crack patterns observed experimentally, as well as the numerical prediction considering only critical stretch, are shown in Figs. 13 (b) and (c). The same limitation is observed, where without the consideration of shear deformation, the XPDM results can not reproduce the experimental observation.

With the consideration of critical shear deformation, the salient features of mixed-mode cracks in rocks under compression are captured. Four wing cracks first initiate from the tip of the notches. Further loading leads to the formation of a strong shear zone located between the two notches, which results in a crack coalescence process between the two pre-cracks. Finally, two shear cracks appear at the outer tip of two notches.

7.2 | Dynamic brittle fracture

7.2.1 | Kalthoff-Whinkler experiment

In this section, a plate with two transverse pre-cracks is considered to illustrate the dynamic performance of XPDM. As shown in Fig. 15 (a), the border nodes between two notches are subjected to a constant velocity of $\dot{u} = 16.54$ m/s. The material parameters are $E = 190$ GPa, $\nu = 0.3$, $\rho = 8000$ kg/m^3. The PD horizon is $\delta = 1.5$ mm, the grid spacing of PD region $\Delta x = 0.5$ mm, the critical energy release rate $G_c = 22.2$ N/mm. As observed from Fig. 15, for two different fitting regions, the average crack

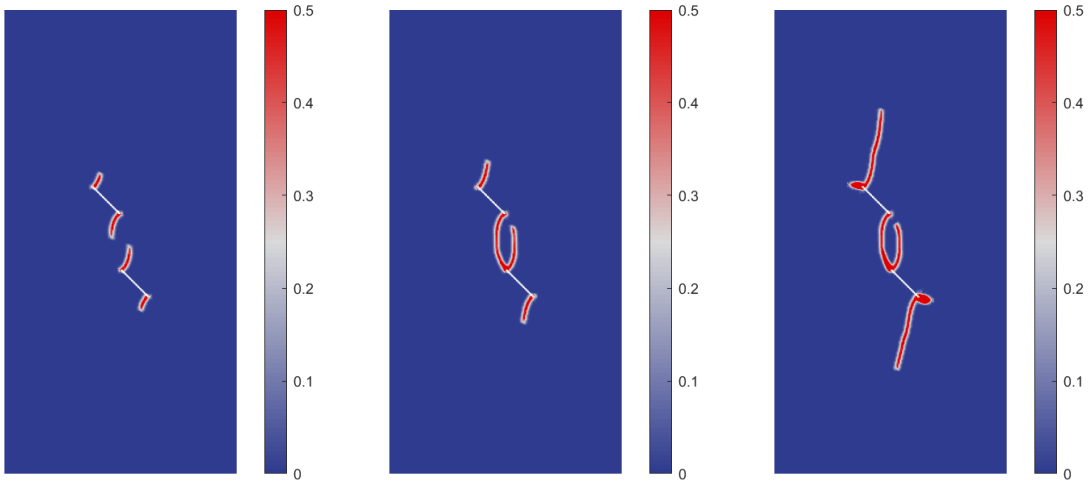

FIGURE 12 Case 1 using XPDM with shear mechanism: F=30.48 kN, F=32.46 kN, F=29.87 kN

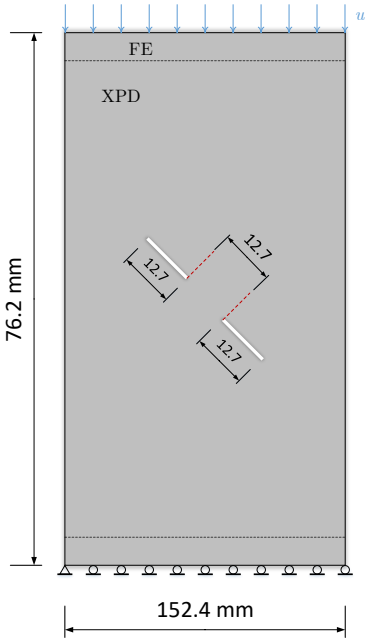

(a) The geometry and boundary conditions

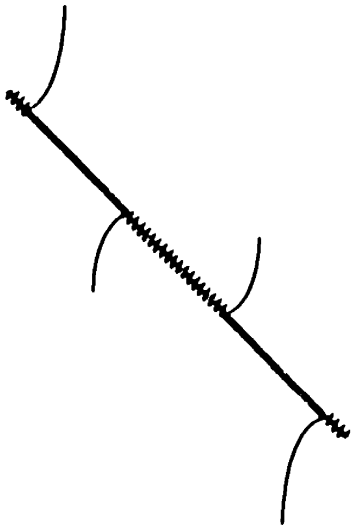

(b) Experimental results

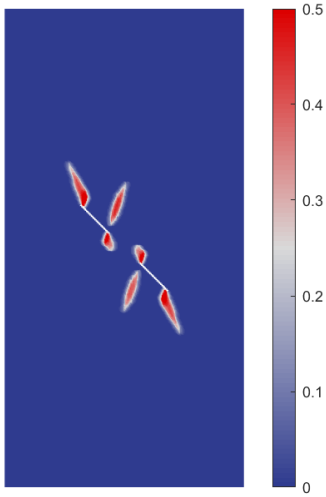

(c) Numerical modeling considering only critical stretch

FIGURE 13 Case 2

extension angles with respect to the horizontal direction are obtained as 69°, comparing well with experiment results[84] (70°), again demonstrating that the size of the fitted domain has negligible effect on the results in this dynamic case.

7.3 | Elastoplastic fracture problems

In this section, three examples are considered to demonstrate the capability of XPDM to accurately reproduce elasto-plastic behavior.

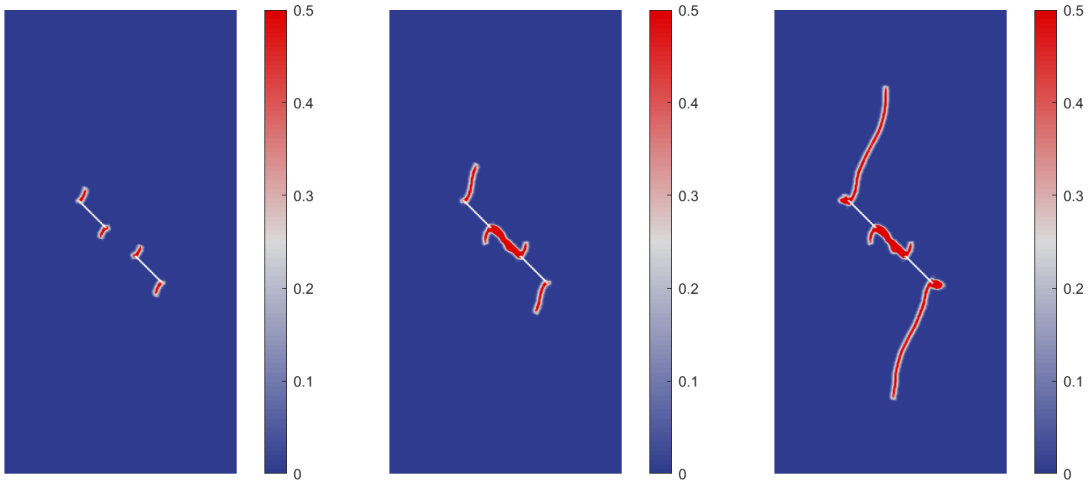

FIGURE 14 Case 2 using XPDM with shear mechanism: F=31.3 kN, F=32.2 kN, F=27.7 kN

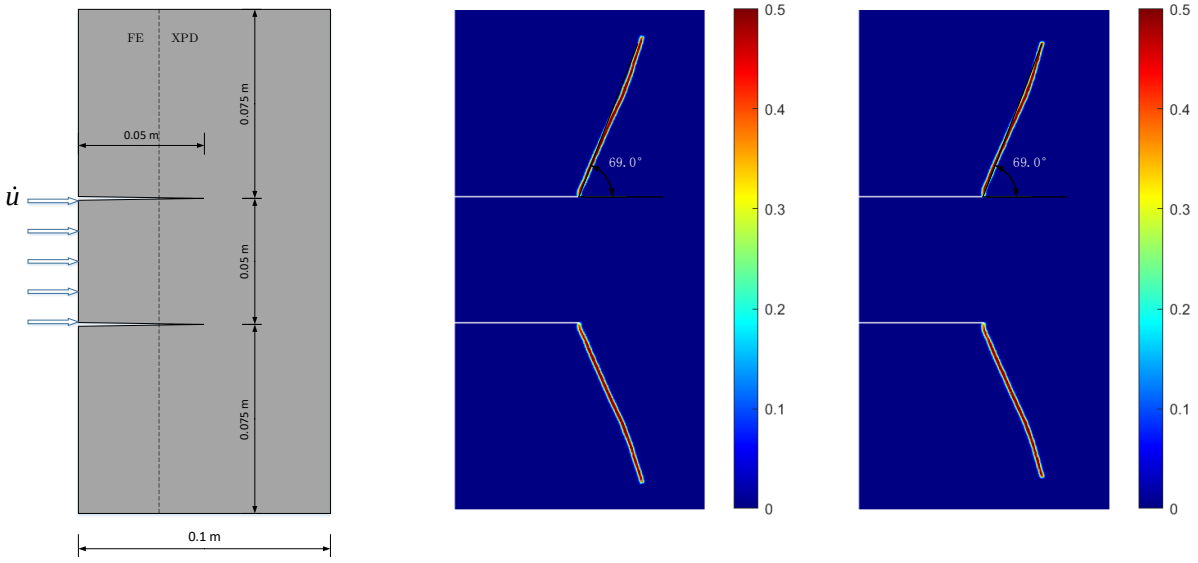

(a) The geometry and boundary conditions (b) XPDM (r=1.5Δx) (c) XPDM (r=3Δx)

FIGURE 15 Kalthoff

7.3.1 | A square specimen subject to compression

In this subsection, we conduct a compression test on a square plate with a side length of 100m under different confining pressures. The central region of the plate is discretized by peridynamic nodes ($\delta = 3$ m, $m = 3$), and the boundary region by a finite element mesh.

TABLE 1 Material parameters for the plate concerning Drucker-Prager yield criterions

E (GPa)	ν	k_0 (MPa)	c_0 (MPa)	φ	τ_c (MPa)	w
10	0.21	/	30	$\frac{\pi}{6}$	12	150

The Drucker-Prager model with hardening is adopted, and the structure is compressed under different confining pressures. The material parameters used for modeling are provided in Table 1. The macro stress-strain curves obtained for different confining pressures are depicted in Figure 16. A close match between the extended peridynamic predictions and finite element results is obtained and the effect of confining pressure on the hardening strength of geomaterials is well demonstrated.

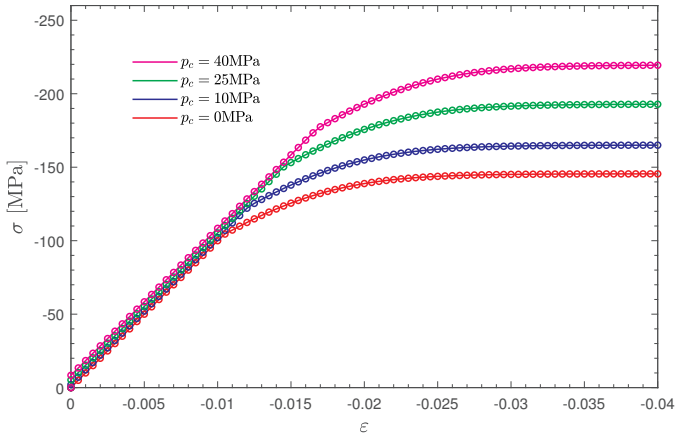

FIGURE 16 Stress-strain curves under different confining pressures, the circle-form symbols are results obtained by FEM and solid lines indicate those computed by XPDM

7.3.2 | Failure prediction in compression tests

Here, a more complicated boundary value problem is considered, where a specimen with tunnel-like holes is subjected to compression. The geometry and loading conditions are presented in Figure 17. The Young's modulus and Poisson's ratio are set as $E = 20$ GPa and $\nu = 0.11$, respectively. The horizon $\delta = 1.5$ m and mesh size equals $\delta/3$. The critical energy release rate is $G_c = 200$N/m, $G_s = 571$N/m, $\beta = 0.8$. The Drucker-Prager type plasticity model is implemented with cohesion $c_0 = 24$ MPa and $\varphi = \frac{\pi}{6}$. The value of the plastic hardening parameters are calibrated as $\tau_c = 24$ MPa and $w = 500$.

The contour maps of the strain field before crack initiation, as predicted by the elastoplastic XPDM and nonlinear FEM are provided in Figures 18 . Figure 19 depicts the displacement of bottom edge of the right tunnel in x_2 direction at $u = 1$m, with a fixed horizon and the decreasing mesh size. It is observed from these comparisons that the XPDM predictions match the FEM solutions closely.

Here, we also demonstrate the formation of a localized shear band in a rock specimen under compressive loadings. The numerical model of rock specimen with a random distribution of initial defects is shown in Fig. 20. The Young's modulus and Poisson's ratio are set as $E = 20$ GPa and $\nu = 0.2$, respectively. The horizon $\delta = 1.5$ mm and mesh size is $\delta/3$. $G_c = 1.5$N/m, $G_s = 4.29$N/m. The Drucker-Prager type plasticity model is implemented with cohesion $c_0 = 25$ MPa. A plastic hardening effect is effected via parameters $\tau_c = 10$ MPa and $w = 500$. The confining pressure $p_c = 15$ MPa. In Fig. 21, the simulation results of the crack pattern are provided. The shear band is formed due to the randomly scattered defects, and the macro-cracks will develop progressively along the shear band.

7.3.3 | Anisotropic plasticity fracture

Geomaterials typically experienced involving mechanical, thermal and chemical actions over a period of time. This geological history may influence a directional bias on the development of microstructural properties, as well as micro defects, to induce an anisotropic effect on the overall mechanical behavior. This sets the backdrop of this subsection, on the development of a simple anisotropic material model. This is similar to existing work on the constitutive modelling of anisotropic behavior, e.g.[85,86], to demonstrate the capability of the model, before venturing into a more mechanism based determination of parameters. We now consider the fracture response of a specimen with an anisotropic plasticity constitutive model 46. As shown in Fig. 22, the specimen with a central hole is subjected to uniaxial tension. This example is adopted to investigate the influence of oriented

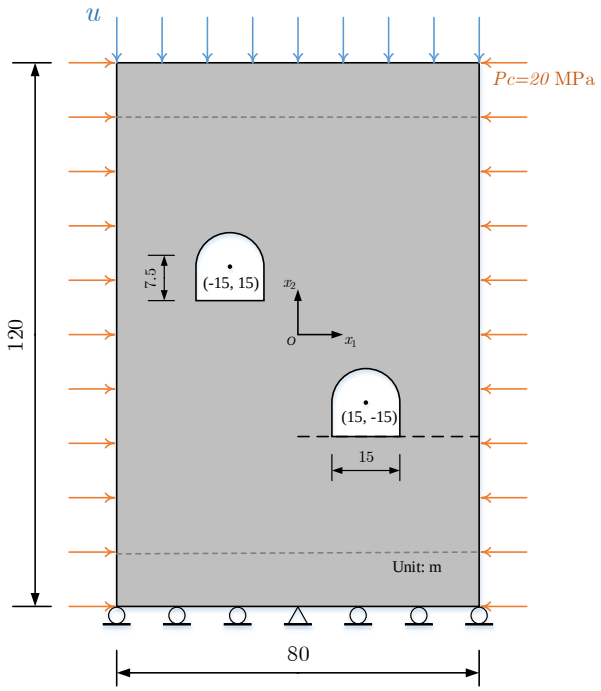

FIGURE 17 The geometry and boundary conditions of the structure

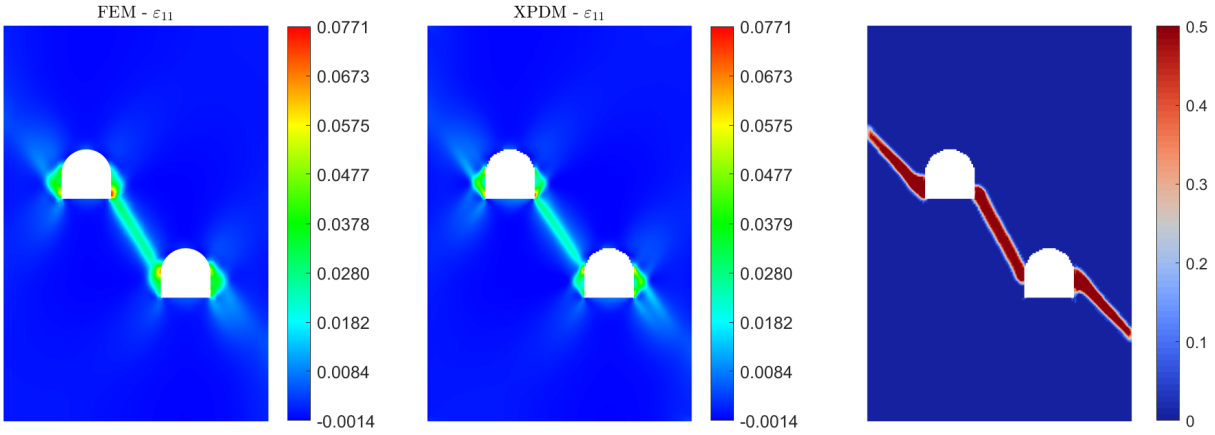

(a) strain field (b) strain field (c) damage field

FIGURE 18 Results obtained by elasto-plastic FEM and XPDM

plastic deformation on the crack propagation direction. The parameters are $E = 30$ GPa and $\nu = 0.2$. The PD horizon 1.5 m and the mesh size is set to 0.5 m, with $G_c = 0.35$N/m, $G_s = 1$N/m, $\beta = 0.5$. The parameters in the anisotropic plasticity constitutive model are: yield stress $k_0 = 10$ MPa, coefficient $\alpha = 10$. In the following, two preferential directions $\boldsymbol{n}_y$ are adopted.

As illustrated in Figs. 23, the strain field is greatly influenced by the orientation defined in the yield function. In Figs. 25 and 26, the crack propagation angle is perpendicular to the direction of plastic flow determined mainly by the unit direction vector $\boldsymbol{n}_y$. In practical applications, the direction vector in the yield function is specified by the user, to reflect the anisotropy of material arising from its underlying micro- and/or meso-structure.

In Fig. 24, the load-displacement curves predicted by elasto-plastic XPD model of different $\boldsymbol{n}$ are provided. As the direction vector changes from horizontal to vertical, the structure will undergo a longer hardening stage and lower strength.

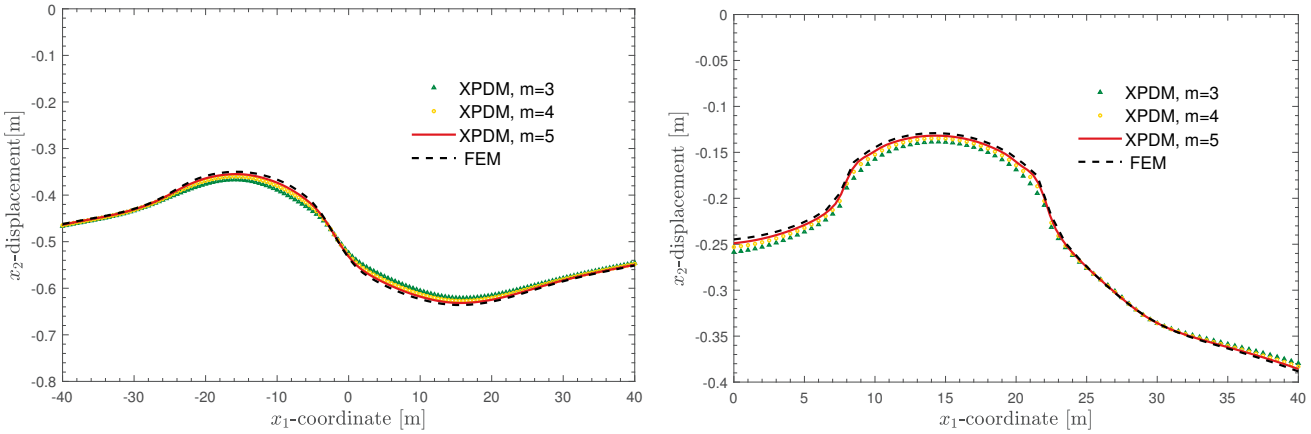

(a) (b)

FIGURE 19 Comparison between elasto-plastic XPDM and FEM in x_2-displacement at $u = 1$m, along (a) the horizontal centerline and (b) the dotted line.

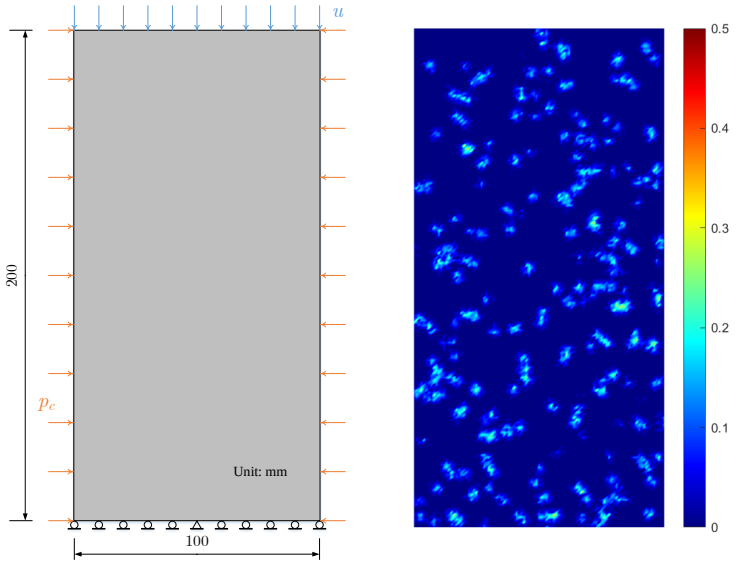

(a) The geometry and boundary conditions (b) Random distribution of initial defects

FIGURE 20 Description of the model

8 | CONCLUSION

In this paper, the predictive ability of XPDM in fracture behavior is investigated for both brittle and elastoplastic material models. With XPDM, different modes of fracture for both static and dynamic problems can be well reproduced. It is found that the bond rotation angle obtained by the strain-based implementation plays a significant role in capturing the complex compressive shear cracks, due to its correct description of shear deformation without the rigid rotation effect. Moreover, the strain-based implementation strategy enables the incorporation of plasticity models into the XPDM framework. The predictive capability of the proposed XPDM method is demonstrated for a wide range of fracture problems in quasi-static and dynamic loading conditions, considering brittle and elastoplastic materials. Despite its excellent problem-solving abilities, more efforts are needed to reduce the relatively high computational consumption caused by its non-local characteristics, such as the application of

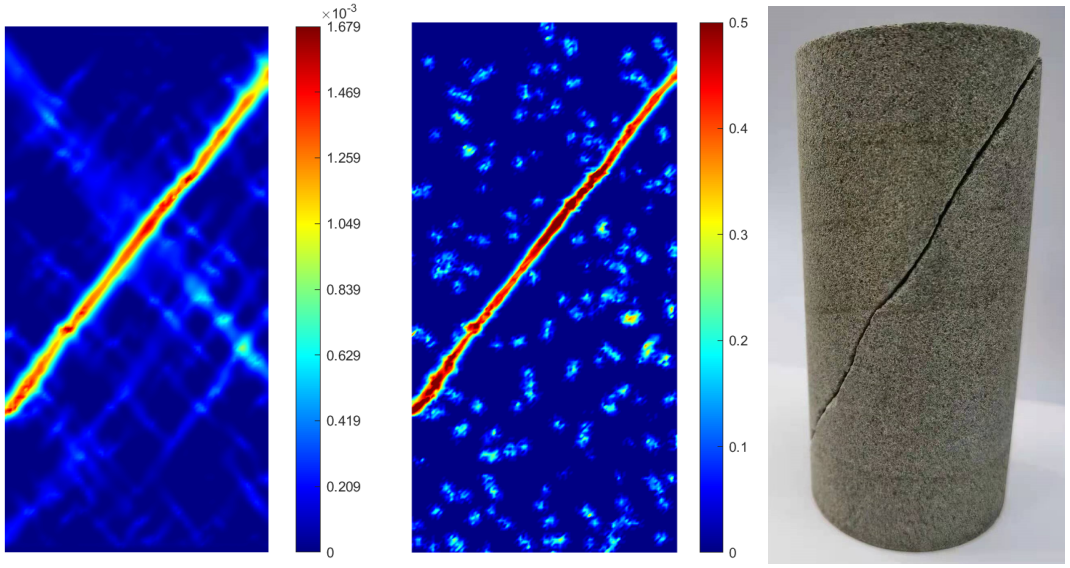

(a) Equivalent plastic strain (b) XPDM damage field (c) Experimental results

FIGURE 21 Comparisons of crack patterns between numerical and experimental results subjected to compression (Confining pressure $p_c = 15$ MPa)

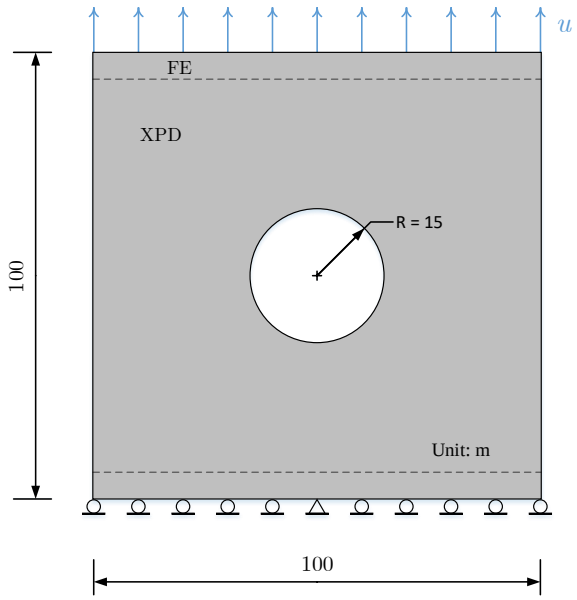

FIGURE 22 The geometry and boundary conditions of the structure

multiscale methods[62,66] to reduce global computational costs, as well as the adoption of parallel programming technique[87] to accelerate the computations.

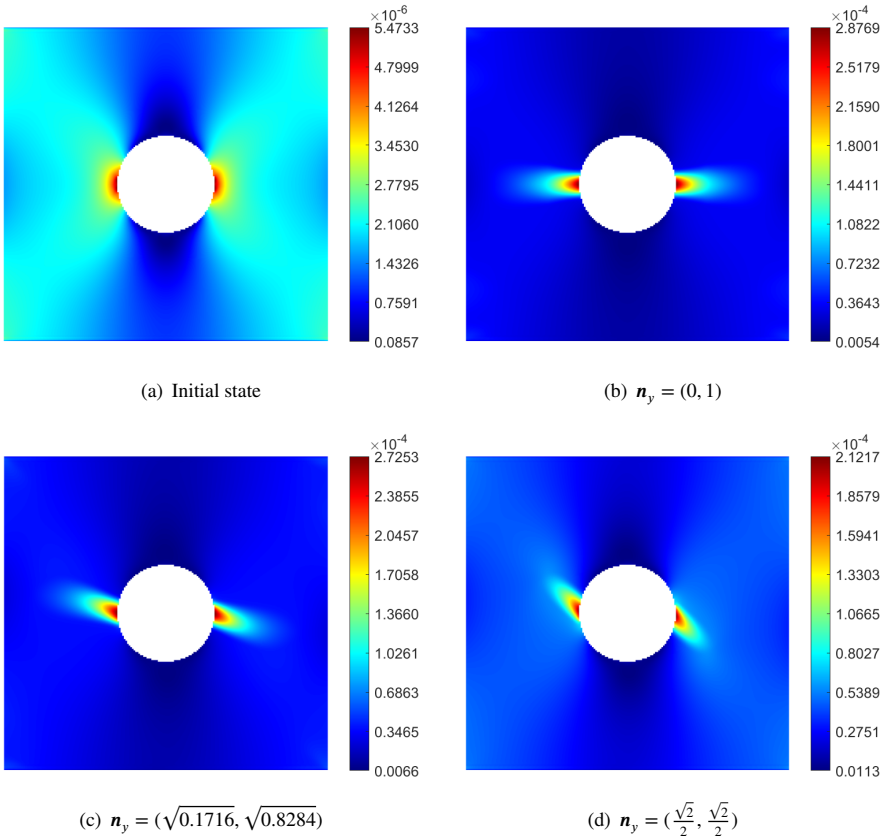

FIGURE 23 Oriented constitutive model, the contour maps of ε_{22} distribution: (a) initial elastic state; (b) (c) (d) the state after extensive plastic deformation right before the crack initiation.

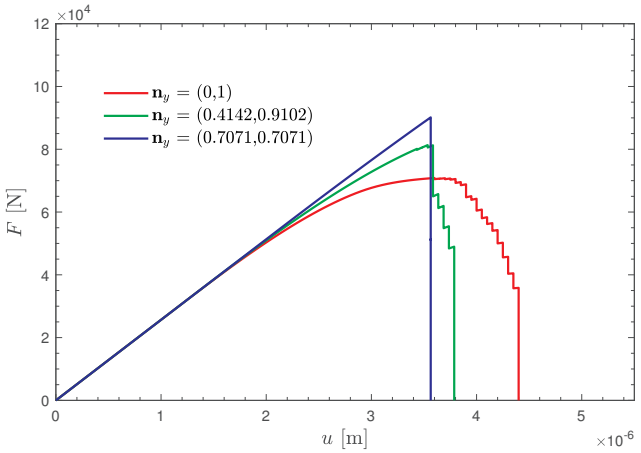

FIGURE 24 Load-displacement curves predicted by elasto-plastic XPDM for different $\boldsymbol{n}$ in yield function ($\delta = 2$ mm).

ACKNOWLEDGMENTS

This work has been jointly supported by the National Key Research and Development Program of China (2017YFC1501100) and the National Natural Science Foundation of China (Grant No. 11872172). This work is also supported by the Fundamental Research Funds for the Central Universities (No. B200203095), China Scholarship Council (No. 202006710097) and the Postgraduate Research & Practice Innovation Program of Jiangsu Province (No. KYCX20_0450).

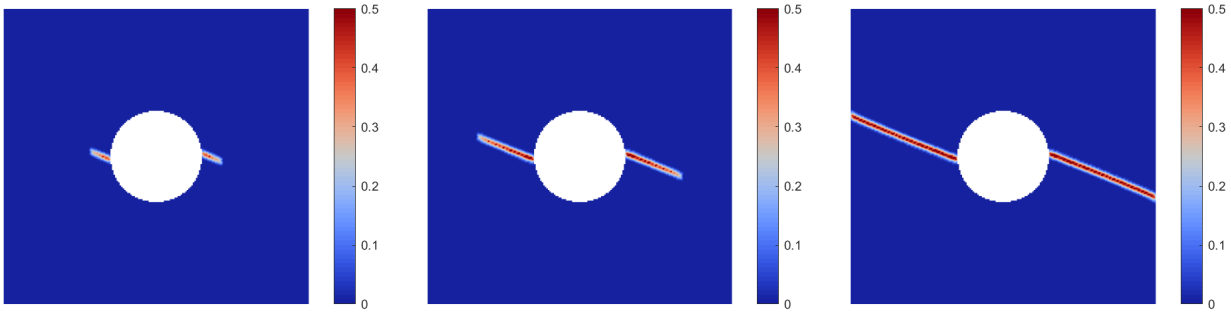

FIGURE 25 Oriented constitutive model, $\boldsymbol{n}_y = (\sqrt{0.1716}, \sqrt{0.8284})$: the crack pattern.

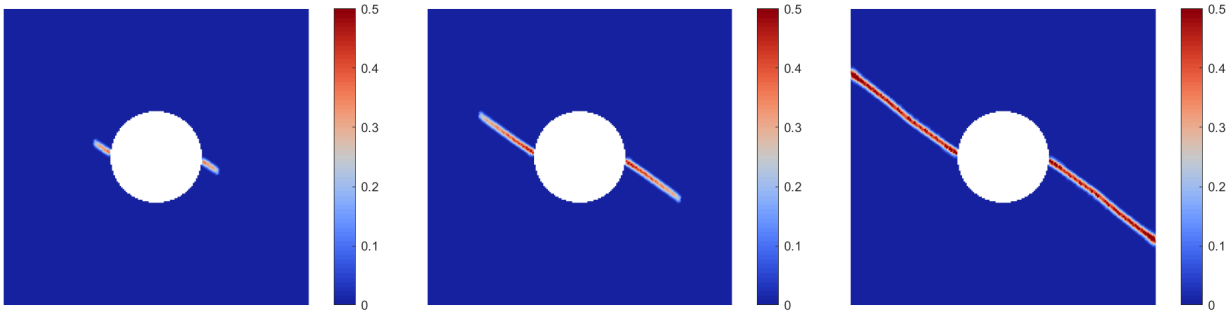

FIGURE 26 Oriented constitutive model, $\boldsymbol{n}_y = (\frac{\sqrt{2}}{2}, \frac{\sqrt{2}}{2})$: the crack pattern.

Conflict of interest

The authors declare no potential conflict of interests.

APPENDIX

A DISCUSSION ON COMPUTATIONAL COST

Here we briefly discuss the computational cost of the extended bond-based peridynamic method and the ordinary state based peridynamics (OS-PD). For a uniform grid in 2D peridynamic numerical model, the number of points associated with each material point is 12 when $\Delta x = \frac{1}{2}\delta$, 28 when $\Delta x = \frac{1}{3}\delta$, 48 when $\Delta x = \frac{1}{4}\delta$. As the horizon δ becomes larger, the bandwidth of the global matrix becomes wider, and the resulting computational cost increases accordingly. With the oridinary state based peridynamic model, the "state" is calculated by integrating the bond stretch within the complete horizon. For the XPDM, the determination of local strain requires only matrix operations on the displacement of the neighboring material points. Accordingly, the XPDM is computationally more efficient than the ordinary state-based model. A quick comparison of computational cost with XPDM and the ordinary state based peridynamics is illustrated in Table A1, where a simple uniaxial tensile example is adopted (the grid and damage pattern are shown in Figure A1). Both methods are numerically implemented in Matlab, using CPU i7-9750H with 6 cores and 12 threads.

TABLE A1 Average computational time (s) required to solve a uniaxial tensile fracture problem in Matlab, using CPU i7-9750H

Number of grid points	XPDM ($\Delta x = \frac{1}{2}\delta$)	XPDM ($\Delta x = \frac{1}{3}\delta$)	OS-PD ($\Delta x = \frac{1}{3}\delta$)
5184	10.1	32.6	37.3
10201	59.5	139	155
40401	746	1272	1436

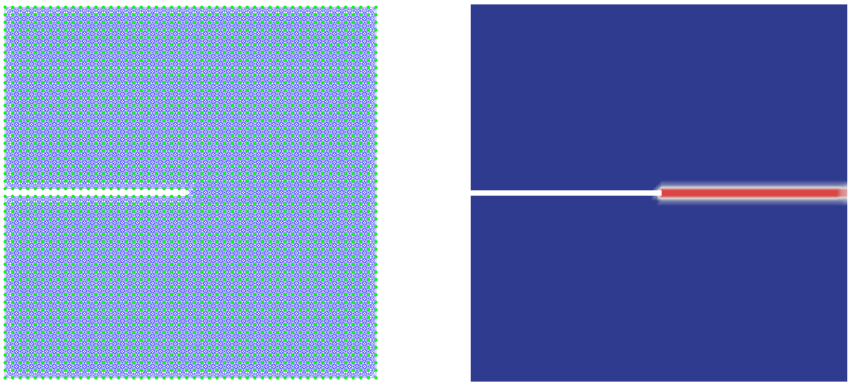

FIGURE A1 The grid and damage pattern.

References

1. Silling S, Askari E. A meshfree method based on the peridynamic model of solid mechanics. *Computers and Structures* 2005; 83(17): 1526-1535.
2. Ganzenmueller G, Hiermaier S, May M. On the similarity of meshless discretizations of Peridynamics and Smooth-Particle Hydrodynamics. *Computers and Structures* 2015; 150: 71-78.
3. Seleson P, Littlewood DJ. Convergence studies in meshfree peridynamic simulations. *Computers and Mathematics with Applications* 2016; 71(11): 2432-2448.
4. Silling S. Reformulation of elasticity theory for discontinuities and long-range forces. *Journal of the Mechanics Physics of Solids* 2000; 48(1): 175-209.
5. Silling S, Lehoucq R. Peridynamic Theory of Solid Mechanics. In: . 44 of *Advances in Applied Mechanics*. Elsevier. 2010 (pp. 73-168).
6. Askari E, Bobaru F, Lehoucq R, Parks M, Silling S, Weckner O. Peridynamics for multiscale materials modeling. *Journal of Physics: Conference Series* 2008; 125: 012078.
7. Madenci E, Oterkus E. *Peridynamic Theory and Its Applications*. Springer, New York . 2014.
8. Zaccariotto M, Luongo F, Sarego G, Galvanetto U. Example of applications of the Peridynamics theory to the solution of the static equilibrium problems. *The Aeronautical Journal* 2015; 119(1216): 677-700.
9. Dayal K, Bhattacharya K. Kinetics of phase transformations in the peridynamic formulation of continuum mechanics. *Journal of the Mechanics and Physics of Solids* 2006; 54(9): 1811-1842.
10. Mikata Y. Analytical solutions of peristatic and peridynamic problems for a 1D infinite rod. *International Journal of Solids and Structures* 2012; 49(21): 2887-2897.

11. Huang D, Lu G, Qiao P. An improved peridynamic approach for quasi-static elastic deformation and brittle fracture analysis. *International Journal of Mechanical Sciences* 2015; 94-95: 111-122.

12. Silling S. Dynamic fracture modeling with a meshfree peridynamic code. In: Bathe K., ed. *Computational Fluid and Solid Mechanics 2003*Oxford: Elsevier Science Ltd. 2003 (pp. 641-644).

13. Ha Y, Bobaru F. Studies of dynamic crack propagation and crack branching with peridynamics. *International Journal of Fracture* 2010; 162(1): 229-244.

14. Youn D, Bobaru F. Characteristics of dynamic brittle fracture captured with peridynamics. *Engineering Fracture Mechanics* 2011; 78(6): 1156-1168.

15. Madenci E, Colavito K, Phan N. Peridynamics for unguided crack growth prediction under mixed-mode loading. *Engineering Fracture Mechanics* 2016; 167: 34-44.

16. Zaccariotto M, Mudric T, Tomasi D, Shojaei A, Galvanetto U. Coupling of FEM meshes with Peridynamic grids. *Computer Methods in Applied Mechanics and Engineering* 2017; 330: 471-497.

17. Madenci E, Barut A, Futch M. Peridynamic differential operator and its applications. *Computer Methods in Applied Mechanics and Engineering* 2016; 304: 408-451.

18. Gao Y, Oterkus S. Multi-phase fluid flow simulation by using peridynamic differential operator. *Ocean Engineering* 2020; 216: 108081.

19. Haghighat E, Bekar AC, Madenci E, Juanes R. A nonlocal physics-informed deep learning framework using the peridynamic differential operator. *Computer Methods in Applied Mechanics and Engineering* 2021; 385: 114012.

20. Shojaei A, Galvanetto U, Rabczuk T, Jenabi A, Zaccariotto M. A generalized finite difference method based on the Peridynamic differential operator for the solution of problems in bounded and unbounded domains. *Computer Methods in Applied Mechanics and Engineering* 2019; 343: 100-126.

21. Bekar AC, Madenci E, Haghighat E. On the solution of hyperbolic equations using the peridynamic differential operator. *Computer Methods in Applied Mechanics and Engineering* 2022; 391: 114574.

22. Zhu QZ, Ni T. Peridynamic formulations enriched with bond rotation effects. *International Journal of Engineering Science* 2017; 121: 118-129.

23. Li WJ, Zhu QZ, Ni T. A local strain-based implementation strategy for the extended peridynamic model with bond rotation. *Computer Methods in Applied Mechanics and Engineering* 2020; 358: 112625.

24. Silling S, Epton M, Weckner O, Xu J, Askari E. Peridynamic States and Constitutive Modeling. *Journal of Elasticity* 2007; 88(2): 151-184.

25. Zhou XP, Wang YT, Shou YD, Kou MM. A novel conjugated bond linear elastic model in bond-based peridynamics for fracture problems under dynamic loads. *Engineering Fracture Mechanics* 2018; 188: 151-183.

26. Wang YT, Zhou XP, Wang Y, Shou YD. A 3-D conjugated bond-pair-based peridynamic formulation for initiation and propagation of cracks in brittle solids. *International Journal of Solids and Structures* 2018; 134: 89-115.

27. Prakash N, Seidel G. A novel two-Parameter linear elastic constitutive model for bond based peridynamics. In: ; 2015; Kissimmee, Florida: 5-9.

28. Zhou XP, Shou YD. Numerical Simulation of Failure of Rock-Like Material Subjected to Compressive Loads Using Improved Peridynamic Method. *International Journal of Geomechanics* 2016; 17(3): 04016086.

29. Hu YL, Madenci E. Bond-Based Peridynamics with an Arbitrary Poisson's Ratio. In: ; 2016; San Diego, California, USA: 4-8.

30. Chowdhury S, Rahaman M, Roy D, Sundaram N. A micropolar peridynamic theory in linear elasticity. *International Journal of Solids and Structures* 2015; 59: 171-182.

31. Zhao GF, Fang J, Zhao J. A 3D distinct lattice spring model for elasticity and dynamic failure. *International Journal for Numerical and Analytical Methods in Geomechanics* 2011; 35(8): 859-885.

32. Diana V, Casolo S. A bond-based micropolar peridynamic model with shear deformability: Elasticity, failure properties and initial yield domains. *International Journal of Solids and Structures* 2019; 160: 201-231.

33. Javili A, McBride A, Steinmann P. Continuum-kinematics-inspired peridynamics. Mechanical problems. *Journal of the Mechanics and Physics of Solids* 2019; 131: 125-146.

34. Zhao GF. Developing a four-dimensional lattice spring model for mechanical responses of solids. *Computer Methods in Applied Mechanics and Engineering* 2017; 315: 881-895.

35. Zhou XP, Tian DL. A novel linear elastic constitutive model for continuum-kinematics-inspired peridynamics. *Computer Methods in Applied Mechanics and Engineering* 2021; 373: 113479.

36. Xu C, Yuan Y, Zhang Y, Xue Y. Peridynamic modeling of prefabricated beams post-cast with steelfiber reinforced high-strength concrete. *Structural Concrete* 2020; 22.

37. Tong Y, Shen W, Shao J, Chen J. A new bond model in peridynamics theory for progressive failure in cohesive brittle materials. *Engineering Fracture Mechanics* 2020; 223: 106767.

38. Madenci E, Barut A, Phan N. Bond-Based Peridynamics with Stretch and Rotation Kinematics for Opening and Shearing Modes of Fracture. *Journal of Peridynamics and Nonlocal Modeling* 2021; 1.

39. Zhang H, Qiao P. Virtual crack closure technique in peridynamic theory. *Computer Methods in Applied Mechanics and Engineering* 2020; 372: 113318.

40. Yu H, Chen X, Sun Y. A generalized bond-based peridynamic model for quasi-brittle materials enriched with bond tension–rotation–shear coupling effects. *Computer Methods in Applied Mechanics and Engineering* 2020; 372: 113405.

41. Zhao H, Zhang X, Qiao PZ. A new peridynamic mixed-mode bond failure model for interface delamination and homogeneous materials fracture analysis. *Computer Methods in Applied Mechanics and Engineering* 2021; 379: 113728.

42. Madenci E, Oterkus S. Ordinary state-based peridynamics for plastic deformation according to von Mises yield criteria with isotropic hardening. *Journal of the Mechanics and Physics of Solids* 2016; 86: 192 - 219.

43. Pashazad H, Kharazi M. A peridynamic plastic model based on von Mises criteria with isotropic, kinematic and mixed hardenings under cyclic loading. *International Journal of Mechanical Sciences* 2019; 156: 182 - 204.

44. Liu Z, Bie Y, Cui Z, Cui X. Ordinary state-based peridynamics for nonlinear hardening plastic materials' deformation and its fracture process. *Engineering Fracture Mechanics* 2020; 223: 106782.

45. Kazemi SR. Plastic deformation due to high-velocity impact using ordinary state-based peridynamic theory. *International Journal of Impact Engineering* 2020; 137: 103470.

46. Ahmadi M, Hosseini-Toudeshky H, Sadighi M. Peridynamic micromechanical modeling of plastic deformation and progressive damage prediction in dual-phase materials. *Engineering Fracture Mechanics* 2020; 235: 107179.

47. Tupek M, Radovitzky R. An extended constitutive correspondence formulation of peridynamics based on nonlinear bond-strain measures. *Journal of the Mechanics and Physics of Solids* 2014; 65: 82-92.

48. Foster JT, Xu X. A generalized, ordinary, finite deformation constitutive correspondence model for peridynamics. *International Journal of Solids and Structures* 2018; 141-142: 245-253.

49. Breitenfeld M, Geubelle P, Weckner O, Silling S. Non-ordinary state-based peridynamic analysis of stationary crack problems. *Computer Methods in Applied Mechanics and Engineering* 2014; 272: 233-250.

50. Wan J, Chen Z, Chu X, Liu H. Improved method for zero-energy mode suppression in peridynamic correspondence model. *Journal of the Mechanics and Physics of Solids* 2019; 35: 1021–1032.

51. Cui H, Li C, Zheng H. A higher-order stress point method for non-ordinary state-based peridynamics. *Engineering Analysis with Boundary Elements* 2020; 117: 104-118.

52. Behzadinasab M. *Peridynamic modeling of large deformation and ductile fracture*. PhD thesis. 2020.

53. Zhou XP, Wang Y. State-of-the-Art Review on the Progressive Failure Characteristics of Geomaterials in Peridynamic Theory. *Journal of Engineering Mechanics* 2021; 147: 03120001.

54. Hu W, Ha YD, Bobaru F, Silling SA. The formulation and computation of the nonlocal J-integral in bond-based peridynamics. *International Journal of Fracture* 2012; 176(2): 195-206.

55. Fung YC. *A First Course in Continuum Mechanics*. PRENTICE HALL, Englewood Cliffs, New Jersey 07632 . 1994.

56. Choo J, Sun W. Coupled phase-field and plasticity modeling of geological materials: From brittle fracture to ductile flow. *Computer Methods in Applied Mechanics and Engineering* 2018; 330: 1-32.

57. You T, Waisman H, Zhu Q. Brittle-ductile failure transition in geomaterials modeled by a modified phase-field method with a varying damage-driving energy coefficient. *International Journal of Plasticity* 2021; 136: 102836.

58. Arriaga M, Waisman H. Stability analysis of the phase-field method for fracture with a general degradation function and plasticity induced crack generation. *Mechanics of Materials* 2018; 116: 33-48.

59. Arriaga M, Waisman H. Multidimensional stability analysis of the phase-field method for fracture with a general degradation function and energy split. *Computational Mechanics* 2018; 61: 181-205.

60. Ni T, Zaccariotto M, Zhu QZ, Galvanetto U. Static solution of crack propagation problems in Peridynamics. *Computer Methods in Applied Mechanics and Engineering* 2019; 346: 126-151.

61. De EA, Peric D, Owen DRJ. *Computational Methods for Plasticity: Theory and Applications*. Wiley . 2008.

62. Galvanetto U, Mudric T, Shojaei A, Zaccariotto M. An effective way to couple FEM meshes and Peridynamics grids for the solution of static equilibrium problems. *Mechanics Research Communications* 2016; 76: 41-47.

63. Kilic B, Madenci E. *Coupling of Peridynamic Theory and Finite Element Method*: 1-12; 2009.

64. Oterkus E, Madenci E, Weckner O, Silling S, Bogert P, Tessler A. Combined finite element and peridynamic analyses for predicting failure in a stiffened composite curved panel with a central slot. *Composite Structures* 2012; 94(3): 839-850.

65. Lee J, Oh SE, Hong JW. Parallel programming of a peridynamics code coupled with finite element method. *International Journal of Fracture* 2017; 203(1): 99-114.

66. Ren HL, Zhuang XY, Cai YC, Rabczuk T. Dual-horizon Peridynamics. *International Journal for Numerical Methods in Engineering* 2016; 108(12): 1451-1476.

67. Ren H, Zhuang X, Rabczuk T. Dual-horizon peridynamics: A stable solution to varying horizons. *Computer Methods in Applied Mechanics and Engineering* 2017; 318: 762-782.

68. Ren H, Zhuang X, Rabczuk T. Implementation of GTN Model in Dual-horizon Peridynamics. *Procedia Engineering* 2017; 197: 224-232.

69. Shojaei A, Zaccariotto M, Galvanetto U. Coupling of 2D discretized Peridynamics with a meshless method based on classical elasticity using switching of nodal behaviour. *Engineering Computations* 2017; 34(5): 1334-1366.

70. Han F, Lubineau G, Azdoud Y, Askari A. A morphing approach to couple state-based peridynamics with classical continuum mechanics. *Computer Methods in Applied Mechanics and Engineering* 2016; 301: 336-358.

71. Tong Y, Shen WQ, Shao JF. An adaptive coupling method of state-based peridynamics theory and finite element method for modeling progressive failure process in cohesive materials. *Computer Methods in Applied Mechanics and Engineering* 2020; 370: 113248.

72. Roth SN, Léger P, Soulaïmani A. A combined XFEM–damage mechanics approach for concrete crack propagation. *Computer Methods in Applied Mechanics and Engineering* 2015; 283: 923-955.

73. Santillan D, Mosquera JC, Cueto-Felgueroso L. Phase-field model for brittle fracture. Validation with experimental results and extension to dam engineering problems. *Engineering Fracture Mechanics* 2017; 178: 109-125.

74. Wu JY, Qiu JF, Nguyen VP, Mandal TK, Zhuang LJ. Computational modeling of localized failure in solids: XFEM vs PF-CZM. *Computer Methods in Applied Mechanics and Engineering* 2019; 345: 618-643.

75. Sudhakar Y, Wall WA. Mesh refitting approach: a simple method to model mixed-mode crack propagation in nonlinear elastic solids. *Advanced Modeling and Simulation in Engineering Sciences* 2017; 4(1).

76. HIRSHIKESH , Natarajan S, Annabattula RK. A FEniCS implementation of the phase field method for quasi-static brittle fracture. *Frontiers of Structural and Civil Engineering* 2019; 13(2).

77. Bouchard P, Bay F, Chastel Y. Numerical modelling of crack propagation: automatic remeshing and comparison of different criteria. *Computer Methods in Applied Mechanics and Engineering* 2003; 192(35): 3887-3908.

78. Bobet A, Einstein H. Fracture coalescence in rock-type materials under uniaxial and biaxial compression. *International Journal of Rock Mechanics and Mining Sciences* 1998; 35(7): 863 - 888.

79. Park C, Bobet A. Crack coalescence in specimens with open and closed flaws: A comparison. *International Journal of Rock Mechanics and Mining Sciences* 2009; 46(5): 819 - 829.

80. Bobet A. *Fracture coalescence in rock materials : experimental observations and numerical predictions*. PhD thesis. 1997.

81. Zhang X, Sloan SW, Vignes C, Sheng D. A modification of the phase-field model for mixed mode crack propagation in rock-like materials. *Computer Methods in Applied Mechanics and Engineering* 2017; 322: 123-136.

82. You T, Zhu QZ, Li PF, Shao JF. Incorporation of tension-compression asymmetry into plastic damage phase-field modeling of quasi brittle geomaterials. *International Journal of Plasticity* 2020; 124: 71 - 95.

83. Wang Y, Zhou X, Shou Y. The modeling of crack propagation and coalescence in rocks under uniaxial compression using the novel conjugated bond-based peridynamics. *International Journal of Mechanical Sciences* 2017; 128-129: 614-643.

84. Kalthoff JF. Modes of dynamic shear failure in solids. *International Journal of Fracture* 2004; 101(1-2): 1-31.

85. Bazant Z, Oh B. Efficient numerical integration on the surface of a sphere. *Journal of Applied Mathematics and Mechanics* 1986; 66(1): 37-49.

86. Giraud A, Huynh Q, Hoxha D, Kondo D. Effective poroelastic properties of transversely isotropic rock-like composites with arbitrarily oriented ellipsoidal inclusions. *Mechanics of Materials* 2007; 39(11): 1006-1024.

87. Mossaiby F, Shojaei A, Zaccariotto M, Galvanetto U. OpenCL implementation of a high performance 3D Peridynamic model on graphics accelerators. *Computers & Mathematics with Applications* 2017; 74(8): 1856-1870.